Numerical study on dynamic icebreaking process of an icebreaker by ordinary state-based Peridynamics and continuous contact detection algorithm

ZHANG Yuan [a, b], TAO Longbin [b], WANG Chao[a*], YE Liyu[a**], GUO Chunyu[a]

[a] College of Shipbuilding Engineering, Harbin Engineering University

[b] Department of Naval Architecture and Marine Engineering, University of Strathclyde

ABSTRACT

The existence of ice and its interaction with structure greatly threaten the navigation of the icebreaker. Due to the damage characteristics of ice, the traditional numerical ways based on mesh method are challenging to solve ice-structure interaction. The nonlocal particle methods have increasingly gained popularity as an essential tool for calculating large deformation problems. In the present work, a meshfree particle-based computational model is developed to investigate the icebreaking process and dynamic icebreaking resistance. The model employs ordinary state-based Peridynamics theory to establish the constitutive relation for ice which is modelled as an isotropic homogeneous elastic material. Furthermore, a continuous contact detection algorithm is proposed, which can be applied to detect the contact process between irregular structures and particles, to study the process of ice-ship interaction. Two dimensional (2D) three-points bending of ice beam and 3D ice sphere impact are studied numerically to validate the method specifically in modelling ice failure. Then, the investigation on the continuous-mode icebreaking process is carried out. The comparison of the present numerical results with existing experimental data demonstrated the validity and accuracy of the present numerical model for analyzing the icebreaking process and predicting the icebreaking resistance.

Key Words： Icebreaking Resistance, Ice failure, Ordinary-state based Peridynamics, Continuous contact detection algorithm；

Nomenclature

V_{ship}	Speed of icebreaker	λ	Scaling factor
L_{WL}	Length waterline of icebreaker	B	Width waterline of icebreaker
B_{WL}	Beam of the waterline of icebreaker	F_x	Force in the direction of the x-axis
F_y	Force in the direction of the y-axis	F_z	Force in the direction of the z-axis
D	Draft of icebreaker	α	Bow waterline angle of icebreaker
ϕ	Bow stem angle of icebreaker	φ	Bow flare angle of icebreaker
ψ	Normal angle	σ_f	Flexural strength
$\boldsymbol{u}$	Displacement vector of the material point $\boldsymbol{x}$	$\boldsymbol{x}$	Position of a material point
$\boldsymbol{u}'$	Displacement vector of the material point $\boldsymbol{x}'$	$\boldsymbol{x}'$	Position of family point of $\boldsymbol{x}$
t	Time	Δt	Time step
ρ	Mass density	$\underline{\boldsymbol{T}}$	Force state
$\boldsymbol{\xi}$	Relative position	$\boldsymbol{\eta}$	Relative displacement
H_x	Family	δ	Internal length (horizon)
s	Bond stretch	s_0	Critical stretch
$\varphi(\boldsymbol{x},t)$	Local damage	G_0	Critical energy release rate
K	Bulk modulus	$\boldsymbol{v}$	Velocity vector
$\mu(\boldsymbol{x},t,\xi)$	History-dependent scalar-valued function	V_p	Volume of the material point
K_I	Fracture toughness	$\boldsymbol{F}$	Force
E	Young's modulus	v	Poisson's ratio
Δx	Particle spacing value	P_k	Control point of the panel
μ	Shear modulus		

1 Introduction

With the increase of arctic activities, such as resources exploitation, investigation work, and transportation, icebreaker plays a pivotal role in ensuring safe navigation and opening channels in ice navigation. Ice loads are regarded as the dominant control force when icebreaker sailing in the common ice condition, level ice, especially in the bow and shoulder area. Ice load will not only damage the structure of the ship but also reduce the navigation performance of the ship. A reliable way to predict the icebreaking resistance accurately of an icebreaker is paramount for the design and safe operation of ice-class ships. However, the engineering performance varied with the environment, and the complex failure mode of ice add challenges to analyze the ice-ship interaction.

The ice-ship interaction process and the ice resistance have been studied using a variety of methods, including experimental measurements, analytical approach, and numerical simulation. Early research on icebreaking resistance was mainly carried out by full-scale measurement (e.g. (Lee et al., 2014; Majid and Menon, 1983; Riska et al., 2001; Sodhi et al., 2001; Williams and Spencer, 1992),) and model-scale test (Derradji-Aouat and van Thiel, 2004; Huang et al., 2018; Huang et al., 2016; Molyneux and Kim, 2007; Shi, 2002). Although the experimental study is the most direct and reliable method to examine the icebreaking ability of icebreakers and observe the ice-ship interaction process (especially the model test), it is often time-consuming and requires considerable manpower, materials, equipment and consequently leads to substantial costs. In addition, it can be difficult to provide sufficient information about the mechanical contact process through experiments. For the ice model test, the scale effect also needs to be further explored and studied (Guo et al., 2016). The approaches for predicting ice resistance in level ice include empirical, semi-empirical, theoretical models, and mostly the combination of the three methods (Liu, 2009). The development is mostly based on three kinds of formulas, i.e., the Lindqvist formula (Lindqvist, 1989) developed based on full-scale tests, Keinonen formulas (Keinonen, 1996) based on a case study of icebreaking vessels, and Riska formulas (Riska et al., 1997). More details of ship hull, ice mechanism, and theoretical analysis were

considered in the study, and this was partly reviewed in detail by researchers (Erceg and Ehlersa, 2017; Kämäräinen, 1993; Li et al., 2018b; Liu et al., 2006).

More recently, Myland and Ehlers (2016) modified the Lindqvist formula by taking two more shape parameters of the ship into account. Jeong et al. (2017) proposed a semi-empirical formula to calculate icebreaker's resistance in level ice, which is a combination of the Lindqvist formula and physical analysis of ice failure process. Also, based on the Lindqvist method, Myland et al. (2019) suggested a semi-empirical model for prediction, which embedded a particle swarm optimization algorithm. This model was applied to study the influence of different encountering conditions on total resistance of the icebreaker. In those models, reasonable simplifications were made, and the empirical coefficients were derived by data fitting from a large number of experiments, including model tests and field tests. Generally speaking, the useful information obtained from the experiments is extremely limited. As a result, these models can only be used to calculate some conventional and straightforward cases with few empirical constants. It is noted that the results calculated based on those formulations vary substantially with the ship size (Erceg and Ehlersa, 2017), which in turn limits their application.

There are some potential numerical methods proposed to investigate the icebreaker's performance in the ice region, including ship motion, ice loads and icebreaking resistance. Combination of the numerical approach with semi-empirical sub-models is one of the common ways. One such method for the ice-load model was firstly developed by Wang (2001), in which contains two vital technical models. One is that a contact algorithm for ice-ship is achieved by the geometric grid method (GM). Another is that the mechanical ice failure process is physically calculated at each contacting step. This model was extended and improved with consideration of a more complex ice-ship contact process and ship motion degrees (Li et al., 2019; Lubbad and Loset, 2011; Su, 2011; Tan, 2014; Zhou et al., 2016). Another model was established by Sawamura et al. (2009), in which the level ice was simulated by a circle contact detection technique. The model was further developed by scholars (Sawamura, 2018; Sawamura

et al., 2015; Sawamura et al., 2017). However, not all of the geometries of the ship hull were investigated by these methods. The other numerical methods modelling the icebreaking processes were either by analytical calculation (Zhou et al., 2018) or by numerical tools, such as Finite Element Method (FEM) (Wang et al., 2014), Discrete Element Method (DEM) (Lau, 2006) and combined Computational Fluid Dynamics (CFD) and FEM (Valanto, 2001). The ice loads calculation in those studies is based on the analytical prediction of ice failure without showing the ice failure mode. Therefore, the development of meshfree methods on ice fracture mechanics and ice-structure interaction has become a newly popular research appraoch, such as Smoothed Particle Hydrodynamics (SPH). Das (2017) simulated ice behaviour in four-points bending by explicit solver LS-DYNA, and this work proves that the SPH method has potential application value in the field of ice damage research. Based on the SPH equation, Zhang et al. (2017) used Drucker-Prager yield surface to model the elastoplastic deformation of ice, and cohesion softening law was embedded to solve the fracture process. Then, a correct SPH method was developed to model structure-ice interaction (Zhang et al., 2019). It can be seen that the SPH method for ice simulation is still in its initial stage of development. In particular, it requires external crack growth criteria to simulate damage (Madenci and Oterkus, 2014; Zhang et al., 2019).

The meshfree method offers several advantages over traditional grid-based approaches (Das et al., 2014), especially in its ability to solve fracture and damage issues in large deformation of structures. Peridynamics (PD), as a nonlocal meshfree method, was initially introduced by Silling (2000). It has strong applicability in engineering problems, including large deformation, damage, fracture, impact, penetration, and instability of both homogeneous and inhomogeneous materials and structures (Madenci and Oterkus, 2014). Moreover, PD can also be applied to subjects other than fracture mechanics (Javili et al., 2019). Many updated mathematical models based on PD theory have been developed over the years: dual-horizon PD was proposed to solve the issue of spurious wave reflections when variable horizons are adopted (Ren et al., 2017); Dual-support SPH was developed in solid within the

framework of variational principle (Ren et al., 2019); the PD differential operator provided a differential form for numerical analysis (Gao and Oterkus, 2020); as well as the combination of PD and FEM model (Madenci et al., 2018) and PD least squares minimization (Madenci et al., 2019). Recently, PD was applied to predict ice-structure interaction for a simple structure interaction with ice (Liu et al., 2017; Lu et al., 2018), which showed PD's potential to study ice fracture. Liu et al. (2018) predicted the ice loads of a ship in rubble ice using the PD theory and Voronoi diagram. A more complex interaction model was introduced to simulate ice-structure contact (Ye et al., 2019; Ye et al., 2017), and the extended work was carried to calculate propeller performance in ice (Wang et al., 2018a). A case of a rigid sphere impacting the ice plate was studied by non-ordinary state-based PD (Song et al., 2019). Recently, ice failure with consideration of fluid is studied by coupling bond-based Peridynamic with updated Lagrangian particle hydrodynamics (Liu et al., 2019). It is worth pointing out that most work reported in the literature has a restriction on Poisson's ratio. This is because bond-based PD employed in these models has the fixed value of Poisson's ratio of 1/3 for 2D and 1/4 for 3D, which is not accurate enough to model ice mechanics since the Poisson's ratio of ice depends on ice temperature and often exceeds 0.33.

Through the above review of the current status of ice-ship interaction, it is noted that the existing models, including empirical formula, semi-empirical method, and grid method of traditional medium mechanics, are able to predict ship's performance as well as ice loads. However, there is a clear weakness among the existing methods in the capability of studying ice failure mechanism or damage evolution in real-time ice-ship interaction. Despite SPH is still in its initial development stage in ice simulation, the PD method offers a clear advantage to handle large deformation and complex fracture patterns. This will contribute to the innovative analysis of the icebreaking process, such as ice failure mode and icebreaking pattern at present work.

Ice is a strain rate-sensitive material (Derradji-Aouat, 2003; Palmer and Dempsey, 2009; Tippmann, 2011). Ice exhibits the mechanical characteristics of ductility under low strain rate loading conditions, and it fails in the form

of creep and microcracks instead of crack formation. Therefore, ice materials can be regarded as viscoelastic plastic materials at low strain rates (Jordaan, 2001; Molyneux, 2017). At high deformation strain rates, i.e., above $\approx 10^{-4} \sim 10^{-3}$, the cracks form and propagate in the ice body which is typically an elastic and brittle process (Schulson, 1990; Schulson, 1999; Schulson, 2001). Normally, the ice is under the action of a high strain rate during the continuous icebreaking process (Derradji-Aouat, 2003; Gao et al., 2015; Molyneux, 2017). In other words, ice can be treated as elastic material and analysed with brittle failure mode when contacting ships. As a result, it is reasonable if the viscous-plastic deformation is not included in the process of ice-ship interaction, and the ice is modelled in the properties of PMB (Prototype Micro-elastic Brittle) for the simulation of ice-ship interaction (Ye et al., 2017). However, a more accurate ice model should be established considering the effects of viscosity and plasticity in future work.

In the present investigation, the ice model is established based on ordinary state-based Peridynamic(OSB-PD) theory, which allows the use of arbitrary Poisson's ratio in the formulation. A continuous contact detection algorithm based on spatial location judgment for ice-ship interaction is introduced, in which the ship is regarded as a rigid body without deformation. The proposed contact detection method can be applied to the contact problem between material particles and any unconventional and complex structural shapes, such as ship hull. Numerical simulation of the icebreaking process and icebreaking resistance is demonstrated in detail by comparing both the model test and the Lindqvist formula calculation. Prior to that, two cases, i.e., a 2D three-points bending of ice beam failure and a 3D ice sphere impact simulation, are conducted to validate the present method in modelling ice failure process.

2 Numerical model

2.1 Framework of ordinary state-based Peridynamics

In PD theory, the continuum is constituted of infinite particles at any instant of time. The main idea of the PD is that the motion information and force information of material points are related to the particles in a certain range

(which is usually known as the horizon). All the particles in the horizon make up the family (The volume occupied by the family is expressed by H_x) of this material point. It can be inferred that each material point has a corresponding family and the interactions with those family members only exist in the horizon. The information on the interactions, such as deformation, force, is stored in different arrays named state. In an undeformed state of the continuum, the selected material point i is located in the global coordinate system, $\boldsymbol{x}$ represents its position in the coordinate system, as shown in Fig. 1. The particles in H_x have interaction with i; for example, the particle j is one of the family members located by the vector $\boldsymbol{x}'$. The horizon of the material point i is described by a circle in 2D (a spherical shape in 3D) with a finite radius δ called internal length. In the deformed state, as shown in Fig. 1, both the material point i and j has a new position $\boldsymbol{y}$ and $\boldsymbol{y}'$. The deformation process of particle points is represented by vectors $\boldsymbol{u}$ and $\boldsymbol{u}'$.

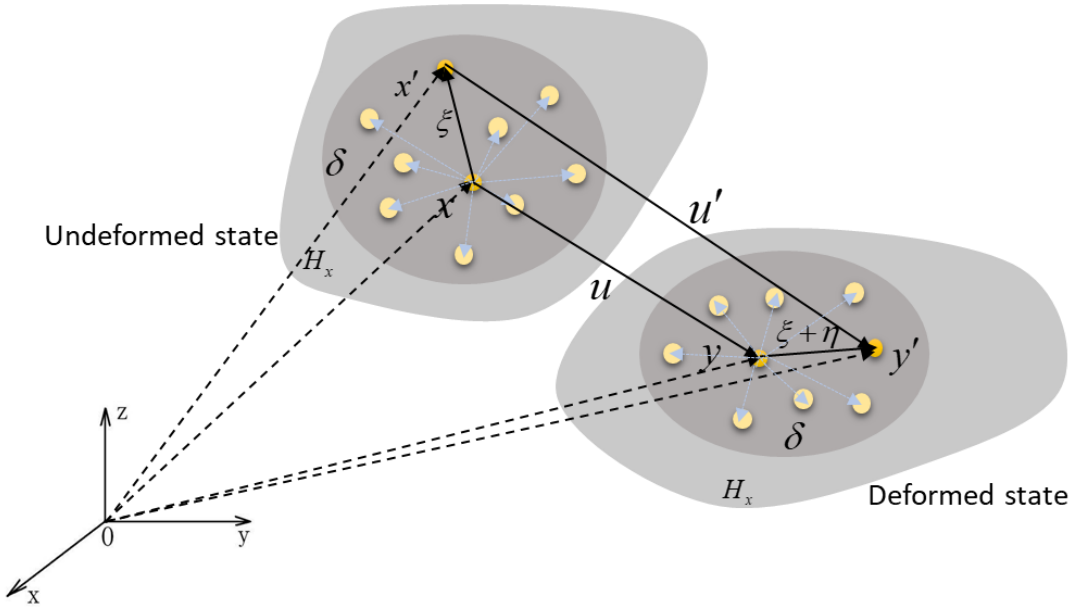

Fig. 1. Material point i interacts with those in the sphere H_x through bonds

Here, $\boldsymbol{\xi} = \boldsymbol{x}' - \boldsymbol{x}$ and $\boldsymbol{\xi} + \boldsymbol{\eta}$, in which $\boldsymbol{\eta} = \boldsymbol{u}(\boldsymbol{x}', t) - \boldsymbol{u}(\boldsymbol{x}, t)$, represent the relative positions of the material points i and j in undeformed state and deformed state, respectively. Then, stretch s describing the deformation can be defined as:

$$s = \frac{|\boldsymbol{y}' - \boldsymbol{y}| - |\boldsymbol{x}' - \boldsymbol{x}|}{|\boldsymbol{x}' - \boldsymbol{x}|} = \frac{|\boldsymbol{\xi} + \boldsymbol{\eta}| - |\boldsymbol{\xi}|}{|\boldsymbol{\xi}|} \tag{1}$$

The PD governing equations is derived as follow (Madenci and Oterkus, 2014; Silling et al., 2007):

$$\rho(\boldsymbol{x})\ddot{\boldsymbol{u}}(\boldsymbol{x},t) = \int_{H_X} \left\{ \underline{\boldsymbol{T}}[\boldsymbol{x},t]\langle \boldsymbol{x}' - \boldsymbol{x} \rangle - \underline{\boldsymbol{T}}[\boldsymbol{x}',t]\langle \boldsymbol{x} - \boldsymbol{x}' \rangle \right\} dV_{x'} + \boldsymbol{b}(\boldsymbol{x},t) \tag{2}$$

Force vector state is given as (Madenci and Oterkus, 2014; Silling et al., 2007):

$$\underline{\boldsymbol{T}} = \underline{t}\underline{\boldsymbol{M}} \tag{3}$$

where M is deformed direction vector state:

$$\boldsymbol{M} = \frac{\boldsymbol{y}' - \boldsymbol{y}}{|\boldsymbol{y}' - \boldsymbol{y}|} \tag{4}$$

Substituting the algebraic formula of force density between particles, which is obtained by partial differentiation of strain energy density, into Eq.(2) can lead to the final expression of the PD governing equation (Madenci and Oterkus, 2014):

$$\rho(\boldsymbol{x})\ddot{\boldsymbol{u}}(\boldsymbol{x},t) = \int_{H_X} \left\{ \frac{2\delta d \Lambda a}{|\boldsymbol{x}' - \boldsymbol{x}|}(\theta + \theta') + 4\delta bs \right\} \boldsymbol{M} dV_{x'} + \boldsymbol{b}(\boldsymbol{x},t) \tag{5}$$

The dilatations θ for material point i, θ' for material point j, are defined as (Gao and Oterkus, 2018; Madenci and Oterkus, 2014):

$$\theta = \int_{H_X} d\delta s \Lambda dV \tag{6a}$$

$$\theta = \int_{H_X} d\delta s \Lambda dV' \tag{6b}$$

where the PD auxiliary parameter, Λ, is defined as:

$$\Lambda = \left(\frac{\boldsymbol{y}' - \boldsymbol{y}}{|\boldsymbol{y}' - \boldsymbol{y}|}\right) \cdot \left(\frac{\boldsymbol{x}' - \boldsymbol{x}}{|\boldsymbol{x}' - \boldsymbol{x}|}\right) = \left(\frac{\boldsymbol{\xi} + \boldsymbol{\eta}}{|\boldsymbol{\xi} + \boldsymbol{\eta}|}\right) \cdot \frac{\boldsymbol{\xi}}{|\boldsymbol{\xi}|} \tag{7}$$

According to Madenci and Oterkus, 2014, the PD parameters a, b, and d in Eq. (5) can be calculated as:

$$a = 0, b = \frac{E}{2A\delta^3}, d = \frac{1}{2A\delta^2} \text{ for 1D} \tag{8a}$$

$$a = \frac{1}{2}(K - 2\mu), b = \frac{6\mu}{\pi h \delta^4}, d = \frac{2}{\pi h \delta^3} \text{ for 2D} \tag{8b}$$

$$a = \frac{1}{2}\left(K - \frac{5}{3}\mu\right), b = \frac{15\mu}{2\pi\delta^5}, d = \frac{9}{4\pi\delta^4} \text{ for 3D} \tag{8c}$$

2.2 Peridynamic failure criterion

In OSB-PD theory, by making the interaction between two particles disappear, the fracture process is then predicted. This process is not reversible once the interaction disappears. Therefore, a recording function Ω is introduced to express the failure of the continuum, that is, whether there is an interaction between two particles. When the value of Ω is true, it indicates that interaction exists between particles, and when the value is false, it means that the force between particles disappears (Madenci and Oterkus, 2014; Silling and Askari, 2005):

$$\Omega(t,\boldsymbol{\xi}) = \begin{cases} 1 & s(t',\boldsymbol{\xi}) < s_0 \\ 0 & s(t',\boldsymbol{\xi}) \geq s_0 \end{cases} \tag{9}$$

in which s_0 represents the critical stretch for interaction between particles in tension condition. It should be noted that ice-structure interaction involves tension failure and compression failure beyond the ice bending test. Generally, ice has compression strength that is 3–4 times its tensile strength (Wang et al., 2018b). Therefore, failure criterion for ice-structure interaction is:

$$\Omega(t,\boldsymbol{\xi}) = \begin{cases} 0 & s(t',\boldsymbol{\xi}) > s_0 \\ 0 & s(t',\boldsymbol{\xi}) < -3s_0 \\ 1 & otherwise \end{cases} \tag{10}$$

The critical stretch value is:

$$s_0 = \begin{cases} \sqrt{\dfrac{G_c}{(3\mu + (\frac{4}{3})^4 (K - 2\mu))\delta}} & \text{for 3D} \\ \sqrt{\dfrac{G_c}{(\frac{6}{\pi}\mu + (\frac{16}{9\pi^2})(K - 2\mu))\delta}} & \text{for 2D} \end{cases} \tag{11}$$

where G_c is energy release rate, and can be expressed by fracture toughness K_I, that is $G_c = {K_I}^2/E$. K is bulk modulus. μ is shear modulus.

In order to quantify the ice failure, a quantity known as local damage is proposed as:

$$\varphi(\boldsymbol{x},t) = 1 - \frac{\int_{H_x} \mu(\boldsymbol{x},t,\xi) dV_\xi}{dV_\xi} \tag{12}$$

The value of $\varphi(\boldsymbol{x},t)$ is between 0-1, and the closer to 1, the greater the degree of the ice damage. $\mu(\boldsymbol{x},t,\xi)$ is a history-dependent scalar-valued function.

3 Contact detection algorithm for ice-ship interaction

In this paper, a method whose function is to calculate the relocation and contact force between an impactor and a PD object is adopted to solve the contact problem (Madenci and Oterkus, 2014). On this basis, a new algorithm based on geometric graphics is developed to detect the contact between material points and a rigid body.

Ice-structure contact is assumed as the impact process between a rigid body and an ice target. The ice target governed by the PD equation moves towards a rigid stationary plate, see Fig. 2 (a). When contact happens, the material points inside the ice body penetrate the rigid body, which is not allowed in the real process, as shown in Fig. 2 (b). Thus, an algorithmic process for the relocation of the coordinates of material points is implemented to reflect reality, as shown in Fig. 2 (c). Ice particles entering the rigid body are relocated to the outside of the impactor surface according to the principle of nearest distance distribution.

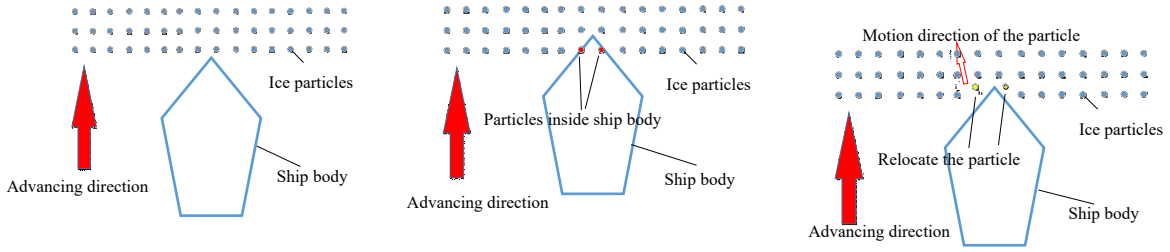

(a) Step, n (b) Step, $n+1$ (c) Step, $n+1$

Fig. 2. Relocation of ice material particle inside the ship body

When the material point $\boldsymbol{x}_{(i)}$ is assigned to its new location, then the velocity at $n+1$ step is calculated as:

$$\boldsymbol{v}_i^{n+1} = \frac{\boldsymbol{u}_i^{n+1} - \boldsymbol{u}_i^n}{\Delta t} \tag{13}$$

In which u_i^{n+1} is the displacement of the relocated material point at $n+1$ step, u_i^n is the displacement of this

material point at time t. Δt represents the time interval of each step. The contact force of ice-structure at $n+1$ step:

$$\boldsymbol{F}_{(i)}^{n+1} = -1 \times \rho_{(i)} \frac{\boldsymbol{v}_i^{n+1} - \boldsymbol{v}_i^n}{\Delta t} V_{(i)} \tag{14}$$

In which $\rho_{(i)}$ and $V_{(i)}$ are density and volume of the particle, respectively. By integrating force of all material points that contacts with the rigid plate, the contact force is obtained:

$$\boldsymbol{F}_{total}^{n+1} = \sum_{k=1} \boldsymbol{F}_{(i)}^{n+1} \lambda_{(i)}^{n+1} \tag{15}$$

Where $\lambda_{(i)}^{n+1}$ indicates the contact state between particles and structure, and is：

$$\lambda_{(i)}^{n+1} = \begin{cases} 1 \text{ inside structure} \\ 0 \text{ outside structure} \end{cases} \tag{16}$$

Thus the reaction velocity and force are calculated by Eq. (14)- Eq. (16). However, the ship hull is a more complex surface rather than a plane or a sphere surface. The judgment of the contact process of ice particles and ship hull is more difficult than that mentioned above. In order to detect the contact between ice particles and the hull surface at each moment, the hull is discretized into a number of elements (see Fig. 3), which can be approximated to the plane elements. Each plane element is expressed as:

$$Ax + By + Cz + D = 0 \tag{17}$$

Then the judgment of the contact between ice and hull surface can be transformed into the judgment of the relative position of particles and quadrilateral surface element. This contact process is performed by the mathematical calculation of the spatial position relations between the points and surfaces (Ye et al., 2019).

For a certain material particle P of ice with coordinate (x_0, y_0, z_0), this point can only collide with one plane element of the hull. For all quadrilateral panels on the hull surface, we can always find its minimum and maximum values of the corners in the three directions, that is $x_{\min}$, $x_{\max}$, $y_{\min}$, $y_{\max}$, $z_{\min}$ and $z_{\max}$. If $x_{\min} < x_0 < x_{\max}$ and $z_{\min} < z_0 < z_{\max}$, or $x_{\min} < x_0 < x_{\max}$ and $y_{\min} < y_0 < y_{\max}$. We consider that these plane elements are possible to collide with the particle P. Then, the nearest plane element to the material point P can be found by calculating

the spatial distances between the point P and these collision-possible plane elements. The contact judgment between the particle and each possible surface element can be expressed as follow:

$$\begin{cases} A_1 x_0 + B_1 y_0 + C_1 z_0 + D_1 \geq 0 & \text{Contact} \\ \text{Otherwise} & \text{No contact} \end{cases} \tag{18}$$

Thus, the process of ice particles-ship hull contact is determined. The particles need to be relocated, and its relocated distance can be determined according to the distance formula of points P and surfaces in space:

$$d = \frac{|\boldsymbol{n} \cdot \boldsymbol{\alpha}|}{|\boldsymbol{n}|} = \frac{|A_1 x_0 + B_1 y_0 + C_1 z_0 + D_1|}{\sqrt{A_1^2 + B_1^2 + C_1^2}} \tag{19}$$

In which $|\boldsymbol{n}|$ is the normal vector of the element. $\boldsymbol{\alpha}$ is the vector passing point on the element surface and the particle P. This process is illustrated in Fig. 3.

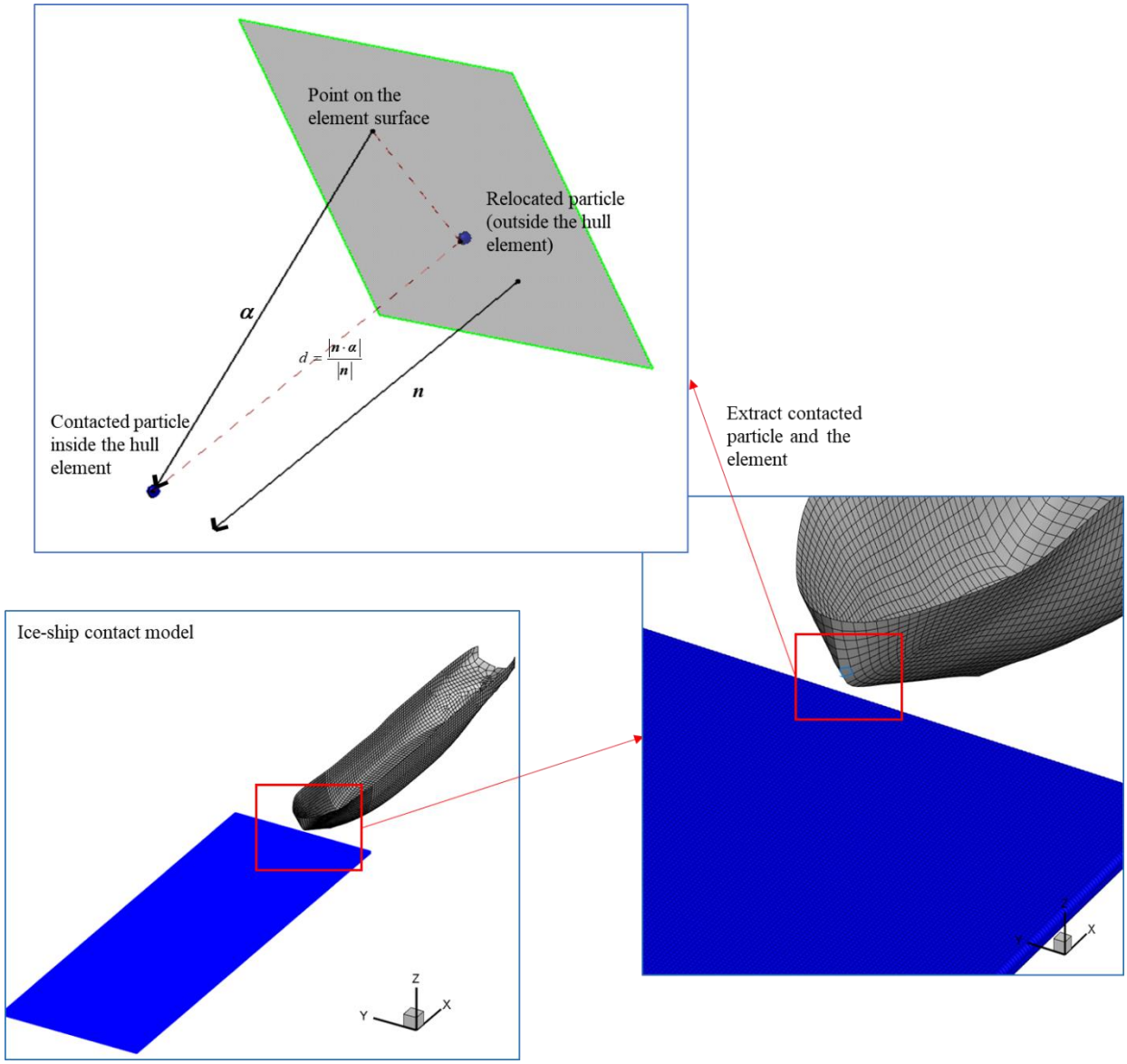

Fig. 3. Detailed relocation procedure when ice-ship contact is detected

The new position of the relocated point $\boldsymbol{x}_{(k)}$ can be calculated by:

$$\boldsymbol{x}_{(k)}^{t+\Delta t} = \boldsymbol{x}_{(k)} + V_{ship} \cdot \Delta t + d \cdot \boldsymbol{n} \tag{20}$$

To reduce the unnecessary contact detection process to achieve efficient calculation, a simple and efficient method to exclude the material points that cannot contact the hull surface is proposed in this work based on Nezami et al. (2004). As shown in Fig. 4, a cuboid is set to enclose the whole ship hull. The length, width, and height of the cuboid equal to the length L, breadth B, and depth D of the ship, respectively. Contact detection algorithm starts only with the ice particle inside the cuboid. It is demonstrated in Fig. 4: Only a tiny part of the ice particles

enter into the cuboid and may collide with the hull. The particles outside the cuboid do not need to enter the contact detection process leading to a considerable reduction in the calculation cost.

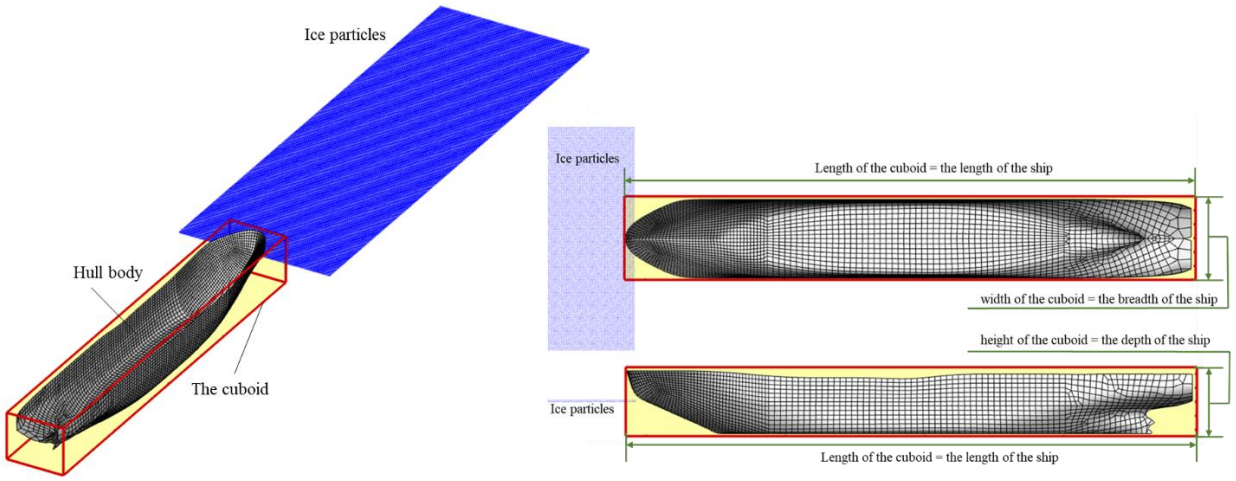

Fig. 4. Illustration of the model to determine the possible contact ice material particles

4 Numerical Strategy

In the numerical implementation, the ice body is discretized into uniform arranged particles. Then the discrete form of Eq.(5) at time step n is:

$$\rho\ddot{\boldsymbol{u}}_i^n = \sum_j \left[\frac{2\delta d \Lambda_{ij}^n a}{\left| \boldsymbol{x}_i^i - \boldsymbol{x}_j^i \right|} (\theta_i^n + \theta_j^n) + 4\delta b s_{ij}^n \right] \Omega(t,\boldsymbol{\xi}) V_j^n + \boldsymbol{b}_i^n \tag{21}$$

where i represents the material point at the current integral step. j is the family members of i.

The contact displacement of ice particles is calculated by the central difference method:

$$\ddot{\boldsymbol{u}}_i^n = \frac{\boldsymbol{u}_i^{n+1} - 2\boldsymbol{u}_i^n + \boldsymbol{u}_i^{n-1}}{\Delta t^2} \tag{22}$$

The discretization of dilatation based on Eq. (6a) is:

$$\theta_i^n = \sum_j d\delta s_{ij}^n \Lambda_{ij}^n \Omega(t,\boldsymbol{\xi}) V_j^n \tag{23}$$

In this study, the surface effects and volume corrections follow the same procedure proposed by Madenci and Oterkus (2014). The horizon δ is set to be $\delta = 3\Delta x$ according to convergence studies conducted by most researchers (Hu et al., 2012; Madenci and Oterkus, 2014; Madenci and Oterkus, 2017; Pashazad and Kharazi, 2019). The boundary conditions of displacement and velocity are imposed according to Oterkus et al. (2014). To obtain

convergent results of explicit time integration scheme, the stability condition is necessary and for the time step size, Δt, is given here (Madenci and Oterkus, 2014):

$$\Delta t < \sqrt{\frac{2\rho_{(i)}}{\sum_j \left(2ad\delta \frac{\left(d\delta \sum_l \left(\frac{1}{\left|\xi_{(l)(i)}\right|} + \frac{1}{\left|\xi_{(l)(j)}\right|} \right) V_{(l)} \right)}{\left|\xi_{(i)(j)}\right|} + \frac{4b\delta}{\left|\xi_{(i)(j)}\right|} \right) (v_{c(j)} V_{(j)})}} \tag{24}$$

The implementation of the program consists of three modules including the main part and two subroutines. The purpose of the main program is to realize the discretization, model processing, and integral calculation of the PD method; one subroutine is used to input the ship node and node numbers obtained from the pre-processing; the last one is the subroutine of contact detection, which transmit the contact pointer $\lambda_{(i)}^{n+1}$ to the main program. The framework of implementation is depicted in Fig. 5.

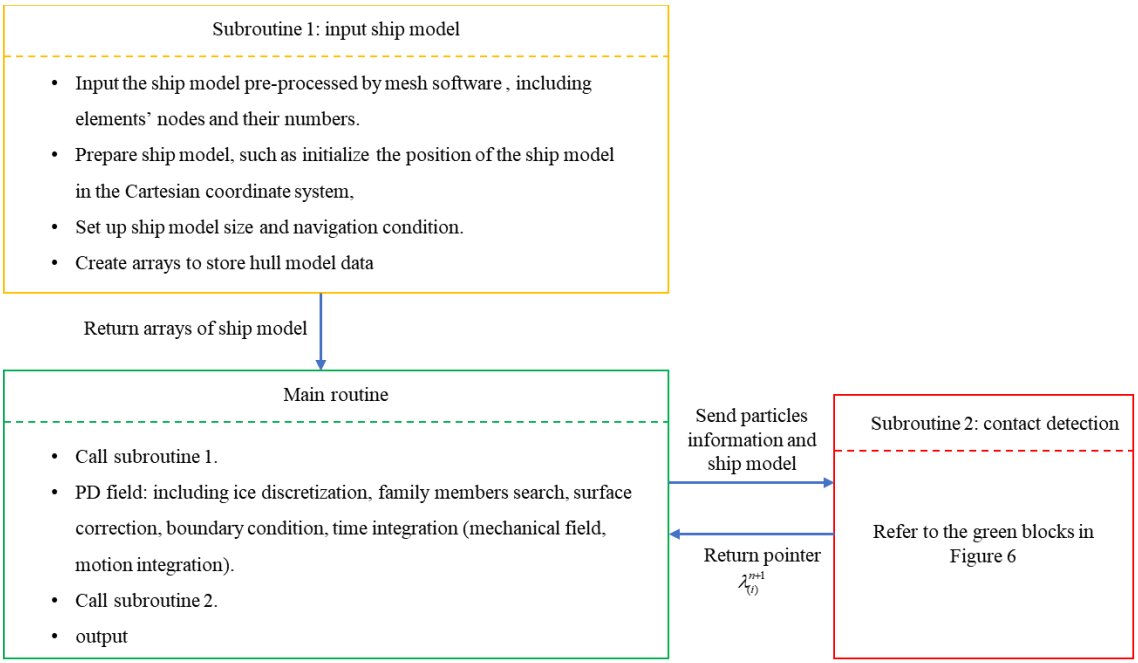

Fig. 5. The framework of the numerical implementation

While constructing the family members, two different arrays are utilized in a conventional way. One is to store all material points inside each particle's horizon, while another is utilized as an indicator for the first array. The family search process is one of the most time-consuming parts of a PD analysis. Especially for problems that require continuous updates of family members inside the horizon of a material point, the time spent searching for family

members becomes crucial (Vazic et al., 2020). The most common algorithm used for family search is the Brute-force search algorithm. However, all material points have to be searched for each point's family in the Brute-force search algorithm, and the time consumed in this process depends on the number of particles. In the present work, the Link-list algorithm (Monaghan, 1985) is applied to determine the array of family members. Link-list search algorithm divides interest domain into numbers of regions by grid. When determining the family of the particle, only the grid, which the particle is located, and its neighbour grids need to be searched. As a result, the computational cost of the family search process is greatly reduced by utilizing the Link-list algorithm.

Fig. 6 is a flow chart of numerical strategy. In Fig. 6, N_t, N_{node}, N_e represents total steps of integral process, the total number of material points in the interest domain, the total number of hull elements, respectively. n represents the current integration step.

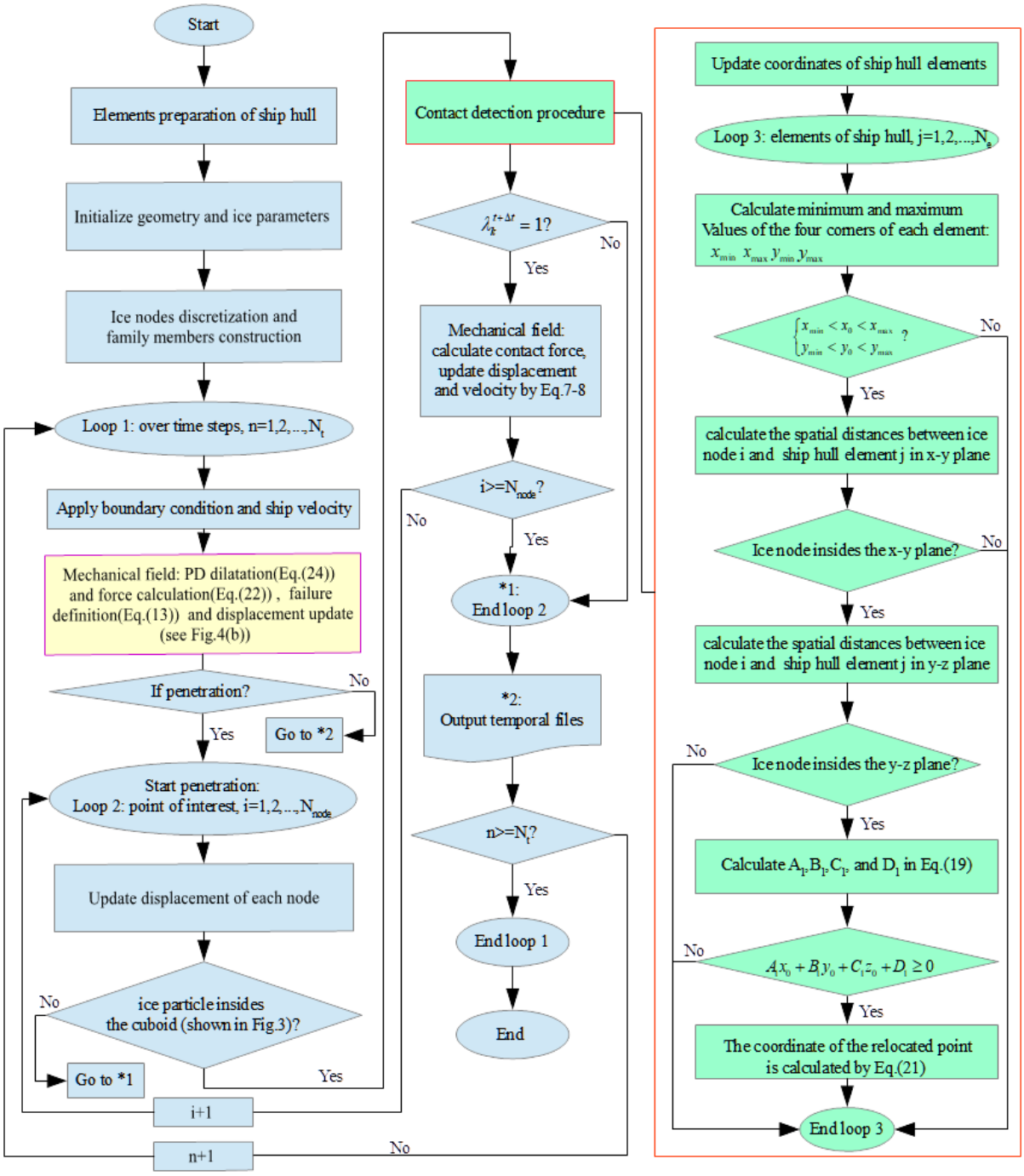

Fig. 6. Flow chart for the numerical strategy

5 Validation of the numerical method in modelling ice failure

In this section, the numerical investigation on the 2D bending process of the ice beam is carried out first to verify the developed model in simulating ice failure. Then, a 3D ice sphere impacting rigid plate is simulated to further demonstrate the ability and efficiency of the proposed model in solving contact process and crack

propagation. The destruction process of the ice is predicted and compared to the test results.

5.1 2D three-points bending of ice beam

Ji et al. (2011) conducted the bending test of the ice beam with a dimension of 700 mm× 75 mm× 75 mm. These experimental results are used as the verification data for the present numerical model. In the test, the ice beam was supported by two fixed bearings in the position of $L_0 = 700\text{mm}$, as shown in Fig. 7. The movable loading head applies the load down from the middle position on the upper side of the ice beam, as shown in Fig. 7. To simulate such a case, the 2D ice beam is discretized into uniformly distributed particles with grid size $\Delta x = 0.005\text{m}$. The rigid supports and leading head are constructed as rigid impactors. The ice beam features are set up the same as the test. Elastic modulus is $E = 1.8\text{GPa}$. Density is $\rho = 900\text{kg/m}^3$. The timestep is set to $\Delta t = 5\times10^{-6}\text{s}$. Poisson's ratio is related to temperature and loading loads which can be calculated as $\upsilon = 0.389$ with temperature -8℃ (Timco et al., 2010). For the critical stretch, the value of $s_0 = 0.001212$ is calculated by Eq. (11) and Eq. (12) with fracture toughness $M_I = 225\text{kPa}\cdot\text{m}^{0.5}$ (Timco et al., 2010). The pre-crack with dimension $a = 10\text{mm}$ is set on the centre line near the bottom to include the initial damage for crack propagating. In the numerical model, the ice beam is set to be a free-moving object, the loading head and support are treated as rigid fix impactors.

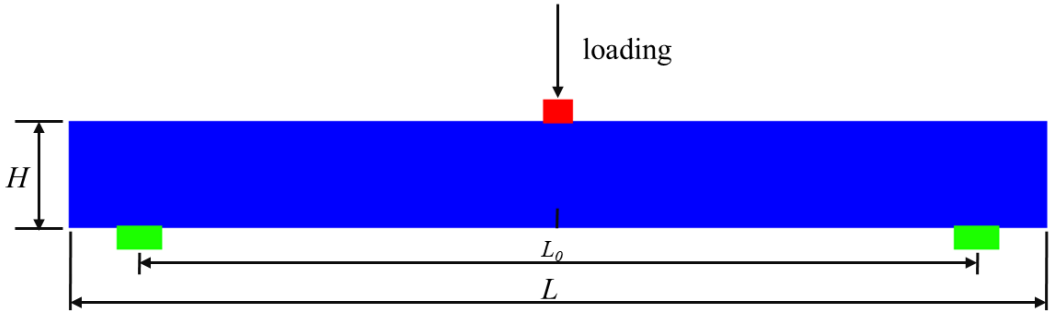

Fig. 7. Numerical model of three-points bending of ice beam

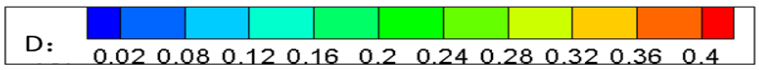

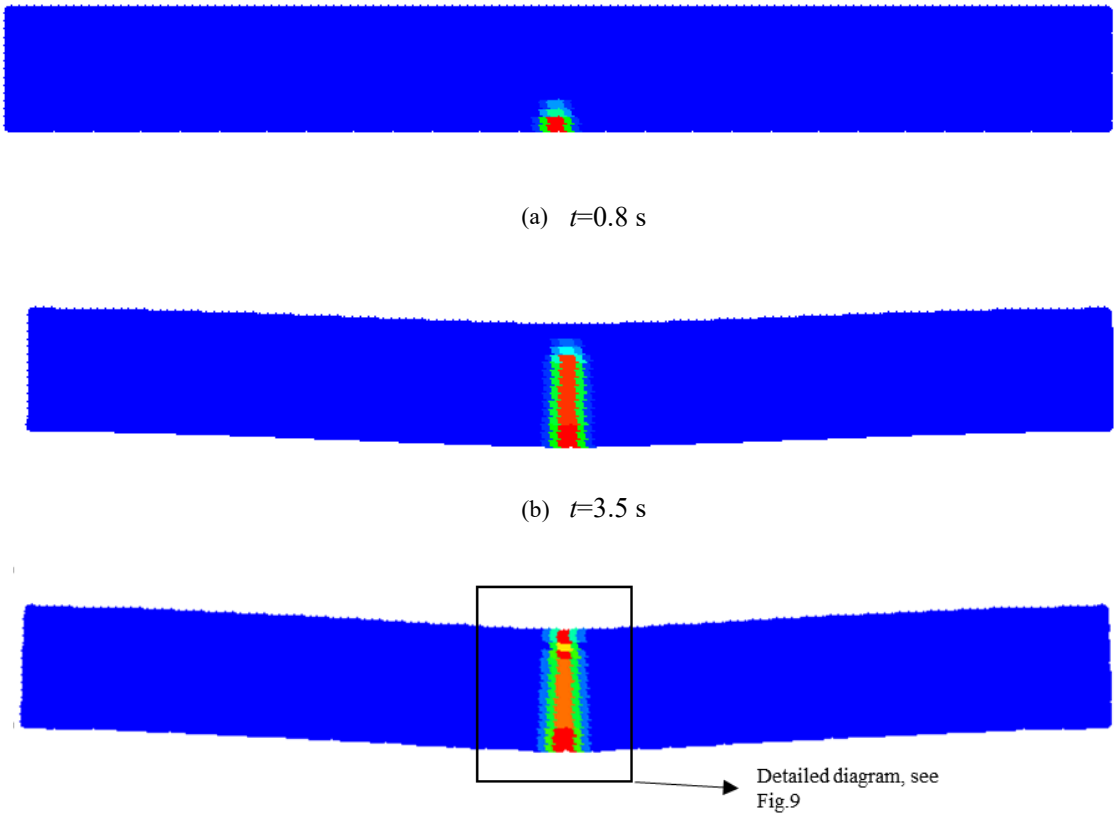

(a) t=0.8 s

(b) t=3.5 s

(c) t=4.3 s

Fig. 8. Contour snapshots of three-points bending of ice beam

The simulation results are shown in Fig. 8, in which (a), (b), and (c) show the contour colour of local damage at 0.8 s, 3.5 s and 4.3 s separately. In contour legend, the D refers to the failure of the ice, which is a quantity calculated by Eq. (13). The failure process of sea ice in the three-points bending mainly goes through three phases. In the first phase, the loading head keeps pressing down at a constant speed, the particles' z-direction displacement in the middle area near the head increases continuously, the z-direction displacement in the two ends of the bar approaches 0. Ice has slight deformation with a small deflection without any damage except for the original crack. The local area beneath the mid-cross section is stretched out. In the second phase, with the increase of the head's displacement, the tension acting on the cross-section of the specimens is strengthened. Damage propagates from the pre-existing crack. The small area damage rapidly expands to the whole mid-cross section, and the material point of the sea ice in the mid-cross section is no longer displaced since they are damaged. Then, both ends of the ice bar

move upward. In the third phase, the ice is subjected to maximum bending strength, and the mid-Cross section is completely destroyed. Fig. 9 is a detailed diagram of the local damage area. It can be observed that the cross-section is nearly smooth, which is in good agreement with the experimental results.

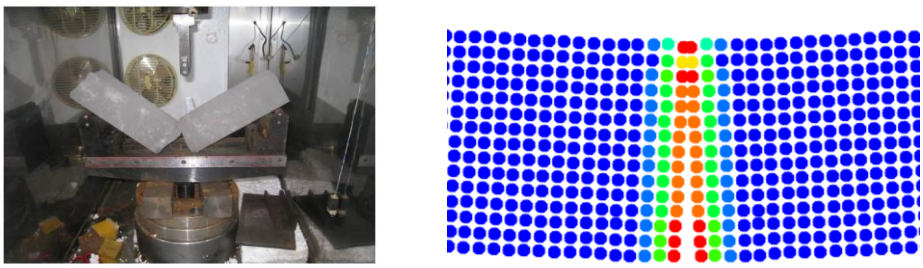

(a) (b)

Fig. 9. Detailed diagram in Fig. 8: (a) experimental snapshot (Ji et al., 2011); (b) numerical simulation

The stress-time curve is shown in Fig. 10, which is a typical elastic-brittle trend. The flexural strength, which is 1.16 MPa measured in the test, is well captured as 1.17 MPa by numerical simulation despite the growth trends at the beginning. The simulation of the three-point bending test of ice shows that the PD method can deal with both the large-scale failure of materials and continuum slight deformation simultaneously.

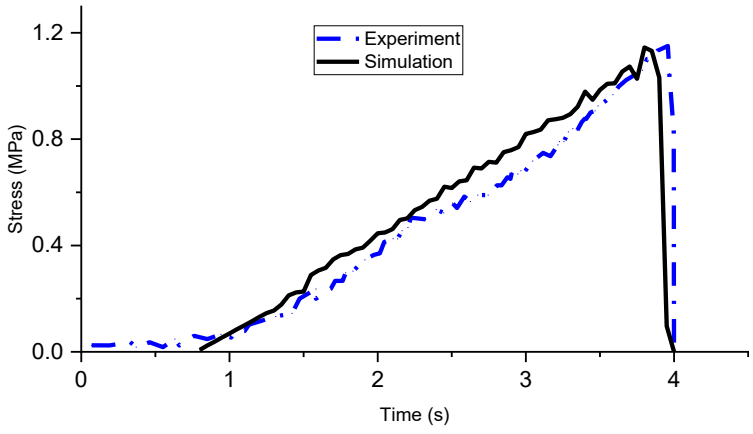

Fig. 10. Comparison of the strain-time curve between numerical results with test data for the three-points bending experiment

5.2 3D Ice sphere impact

Impact studies with PD are widely studied by bond-based PD without a pre-existing crack (Parks et al., 2008;

Ruestes et al., 2014; Silling and Askari, 2005; Ye et al., 2019). Note that there is also no initial damage in this sphere impact model. The impact case is carried out on an ice impact problem with high speed (Tippmann et al., 2013).

The initial snapshot of an ice sphere with a diameter $D_{sphere} = 61\text{mm}$ impacting a rigid flat panel at high speed of $V = 61.8\ \text{m/s}$ is shown in Fig. 13 (a) (right). The ice sphere is treated as isotropic homogeneous elastic material with a density of $\rho = 900\text{kg/m}^3$, a Poisson's ratio of $\upsilon = 0.33$, and an elastic modulus of $E = 1.8\text{GPa}$. The critical stretch is 0.003133. The time step is $\Delta t = 1*10^{-7}\text{s}$. In the numerical model, the ice sphere is set to be a free-moving object, and the flat panel is treated as a rigid fix impactor.

In the PD theory, it is crucial to determine grid size Δx and the horizon size δ to achieve high accuracy with sufficiently small amount of computational time. These two variables can be obtained by the *m*-convergence study and the *δ*-convergence study, in which $\delta = \Delta x \cdot m$. However, *m* is suggested to be 3 or 3.015 in most PD application literature (Madenci and Oterkus, 2014; Silling and Askari, 2005; Wang et al., 2020). Moreover, the PD application in ice simulation (Vazic et al., 2019; Wang et al., 2018a; Zhang et al., 2020) has also demonstrated that the 3.015 is the optimum value for *m*. Therefore, $m = 3.015$ is chosen in the present study. The convergence study of δ is also carried out with the horizon sizes being set to $\delta = 4.5979mm$, $\delta = 6.1305mm$, $\delta = 9.1957mm$, $\delta = 18.3915mm$ corresponding to $\Delta x = D/40$, $\Delta x = D/30$, $\Delta x = D/20$, $\Delta x = D/10$, respectively. Fig. 11 and Fig. 12 depict the ice sphere failure and time-history impacting force.

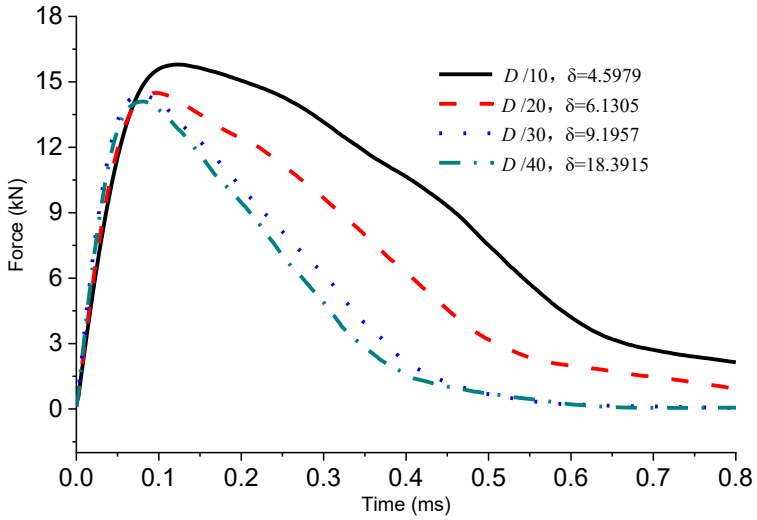

Fig. 11. Impact loads with different particle spacing

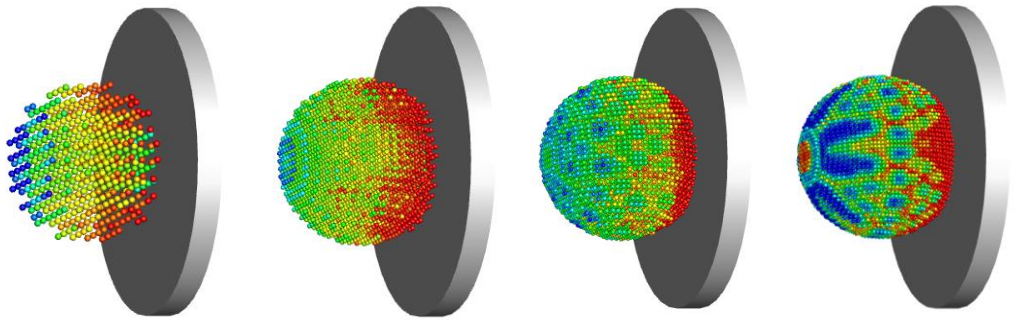

（a） $\delta = 4.5979\text{mm}$ b） $\delta = 6.1305\text{mm}$ （c） $\delta = 9.1957\text{mm}$ （d） $\delta = 4.5979\text{mm}$

Fig. 12. Ice spere failure with different particle spacing at $t = 120\mu\text{s}$

As shown in Fig. 11, the impact forces are in a high degree of a coincidence for $\delta = 4.5979mm$ and $\delta = 6.1305mm$. However, it can be seen that the cracks are not propagating well when $\delta = 6.1305mm$, as shown in Fig 12 (d). Thus, $\delta = 4.5979mm$ is subsequently chosen for further study.

Fig. 13 shows a series of snapshots of the dynamic impact process of the ice sphere from experimental photographs (Tippmann et al., 2013) and the present numerical results at different times. The contour legend of ice failure in the PD simulation is shown above the figure. Both the test and numerical results clearly demonstrate the initiation of contact, fracture of sphere body and the evolution of the crack. Local fragmentation at the contact face begins at 40 μs in Fig. 13 (b), which is captured by the present PD simulation, and the level of ice failure are shown

clearly in the PD simulation by local damage (Eq.(12)). Cracks, perpendicular to the contact surface, continue to travel in this direction from 40 μs to 120 μs. Except for local damage at the contact face, the ice spherical maintains a relatively complete shape at the first 120 μs. During this period, the strip crack extends rapidly from the contact surface to the left side of the ice sphere, which is shown in green particles in the PD simulation. By the time step of 760 μs, the sphere has lost its shape and broke into small fragments and powder spray. Minor units in the PD model are particles, so the fully damaged red independent particles in the contact surface can be regarded as a diffused powder displayed in experimental photos. It can also be found that the fragmentation of the ice sphere becomes more severe with time.

As shown in Fig. 13, the present model and contact detection algorithms are reliable to model the ice impacting damage and fracture evolution. Different damage patterns are observed, similar to those observed in experiments. It is shown that the PD model has an advanced ability to simulate ice failure.

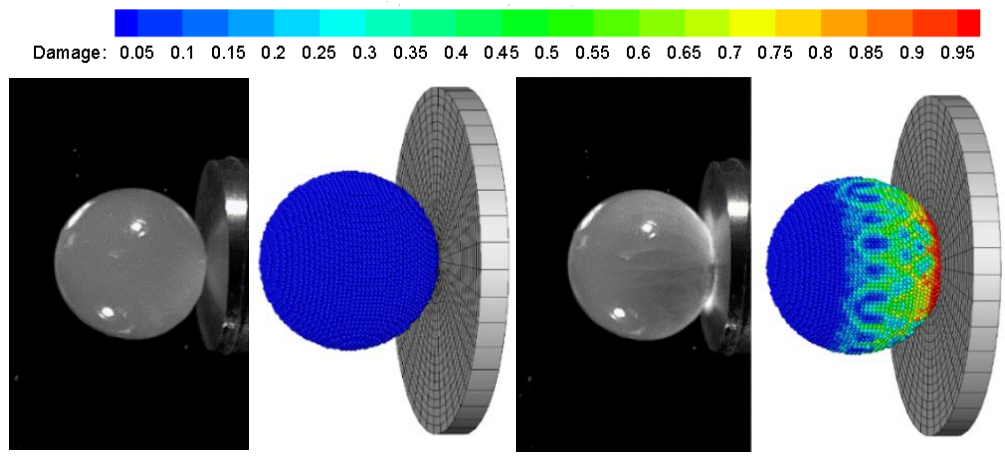

(a) t=0 μs (b) t=40 μs

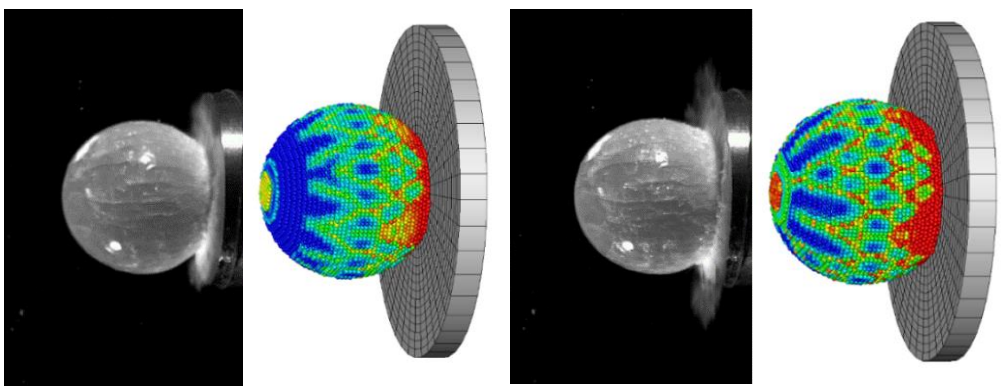

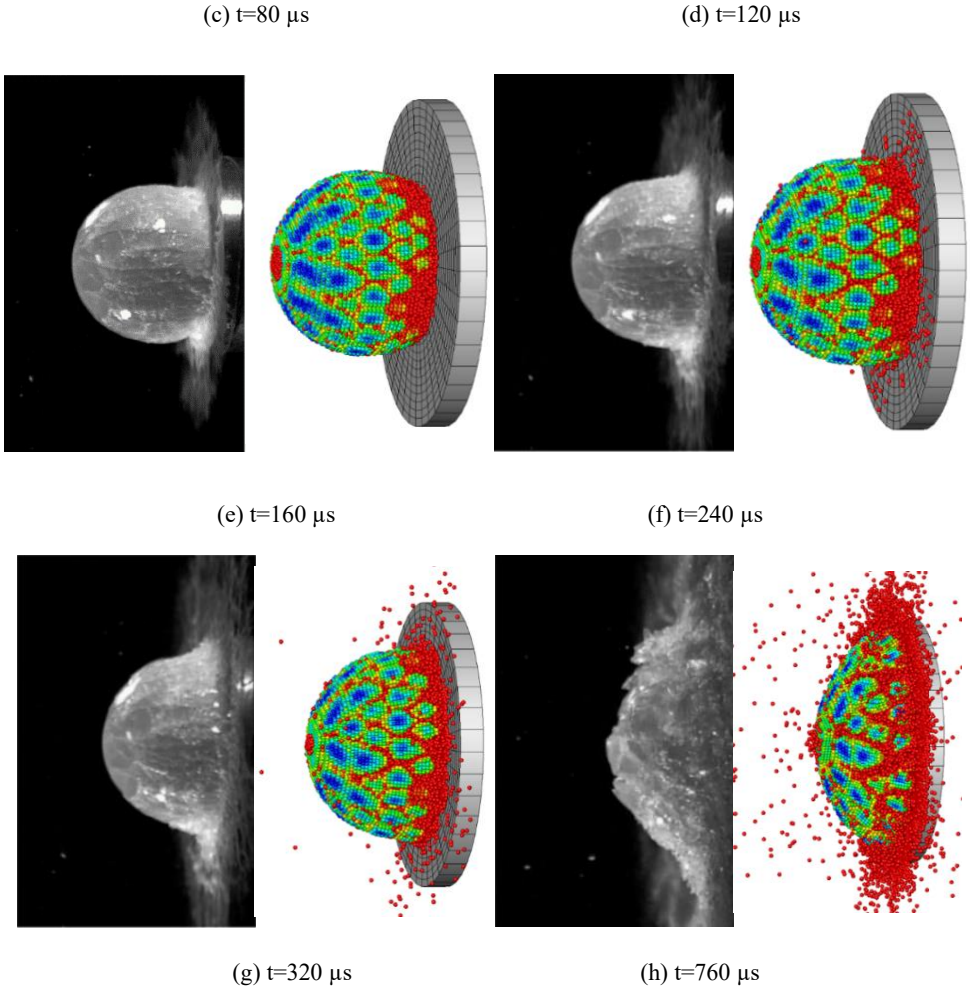

Fig. 13. Comparisons of the failure progress of the dynamic impact of the ice sphere between test photographs (Tippmann et al., 2013) (left) and the PD numerical simulation snapshots (right)

6 Numerical simulation of icebreaking resistance

The average fashions are usually used to describe the resistance force in the ice-ship interaction process. Amongst those the most well-known and acceptable is the form proposed by Riska (Riska, 2011). The resistance force is divided into breaking ice forces, submerging broken ice forces, friction forces along the ship hull (both ice floes breaking and sliding along the hull) and hydrodynamic forces. The breaking force plays a vital role in lower speed conditions, and it contributes over 50% of the resistance. Furthermore, ice failure is complex since it consists of a multi-mode failure process, including crushing, bending, buckling and shearing (Fig. 14), in which bending and

crushing are common failure patterns and are modelled by the PMB model in the present work. However, the visco-plastic model is also needed in future work to study very initial contact between ice and ship deeply.

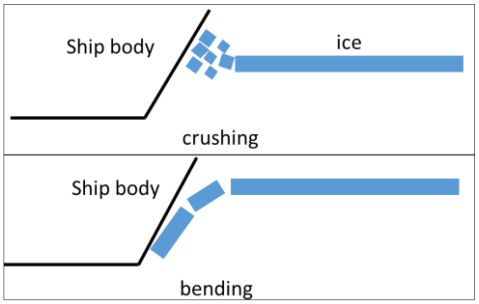

Fig. 14. Two main failure patterns of the icebreaking process

The present work focuses on ice failure process and dynamic icebreaking loads in continuous-mode icebreaking in level ice. In this part, the icebreaking process of ice-ship interaction is considered based on PD theory and continuous contact detection algorithm, and icebreaking resistance acting on the ship hull is investigated. The scale ratio of 1:40 for the icebreaker is adopted in the numerical model, and the working condition is the same as the model test. It should be noted that the hydrodynamic effect of ice floes after breaking has not been discussed yet. However, the prediction of icebreaking resistance and ice failure pattern in this paper is still reasonable by the validation with the experiment.

6.1 Model test description

The model test was carried out at the Ice Engineering Laboratory of Tianjin University. Test facilities and model ice are described in (Huang et al., 2016). The study object is an icebreaker with a scaling factor λ=40, showing in Fig.15. And the main parameters of the icebreaker are shown in Table 1. A tactile sensor was used to measure the distribution and variation of the ice load on the bow region in model tests. It is a total of 464 mm in length and 464 mm in width and is formed of 1024 sensing elements (each 14.5 × 14.5 mm) arranged on a soft sheet. According to field measured data and scale factor, the required ice conditions at the model scale are 37.5 mm in thickness and 12.5 KPa in flexural strength, respectively.

Fig. 15. Icebreaker model

Table 1. Parameter for full scale and model scale of icebreaker

Parameters	Full scale	Model scale
Length waterline (L_{WL}) (m)	155	3.875
Beam of WL(B_{WL}) (m)	23	0.575
Draft (D) (m)	9	0.225
Bow waterline angle α (deg)	22	22
Bow stem angle ϕ (deg)	24	24
Bow flare angle φ (deg)	40	40
Navigating speeds V_{ship}	1kn, 2 kn, 3 kn, 4 kn and 5 kn	0.082m/s, 0.164 m/s, 0.246 m/s, 0.328 m/s and 0.410 m/s

6.2 Geometry and numerical setup

For the hull model, it is simplified to a rigid body and discretized into a series of quadrilateral elements which are used to detect contact between ship hull and ice particles. Since the shape in the bow region is relatively complicated, and the ice force of ice-bow interaction contributes the most icebreaking resistance, the quadrilateral elements in this area are refined, as shown in Fig. 17.

As illustrated in Fig. 18, in the configuration of the initial ice-ship interaction model, level ice is $L_{ice} = 6\text{m}$ in length, $B_{ice} = 4.8\text{m}$ in width, and thickness $H_{ice} = 0.0375\text{m}$ (the same with the model test). The right and left

sides along the forward direction of the ice model are set to be fixed boundaries. Spacing between two ice particles is set to be $\Delta x = H_{ice} / 3\text{m}$. Therefore, the volume of each particle is calculated as $\Delta V = 1.95 * 10^{-6}\text{m}^3$. The engineering properties of ice are also listed here, e.g., the density of ice $\rho = 900.0\text{kg/m}^3$, the elastic modulus is set to be $E = 25.0\text{MPa}$, which is 2000 times the flexural strength (Molyneux, 2017). Poisson's ratio $\nu = 0.33$. The time step is $\Delta t = 1 * 10^4\text{s}$.

At first, the mesh convergence studies for determining the best hull element size are carried out with the icebreaker breaking the ice at its velocity of $V_{ship} = 0.41\text{m/s}$. The basic mesh sizes are $L_{WL}/180$, $L_{WL}/220$, and $L_{WL}/100$. The icebreaking force in the *x*-direction is plotted in Fig. 16. it can be seen that the force curves with size $L_{WL}/220$ and size $L_{WL}/180$ are almost coincident, and their mean values are 12.2 N and 13.6 N, respectively. Although the force curve with size $L_{WL}/100$ has a similar trend, it has more peaks and a larger mean value of 17.2 N. Therefore, the mesh sizes $L_{WL}/220$ and $L_{WL}/180$ are enough to describe the ship hull. In this work, the mesh size $L_{WL}/180$ is set in the ship model.

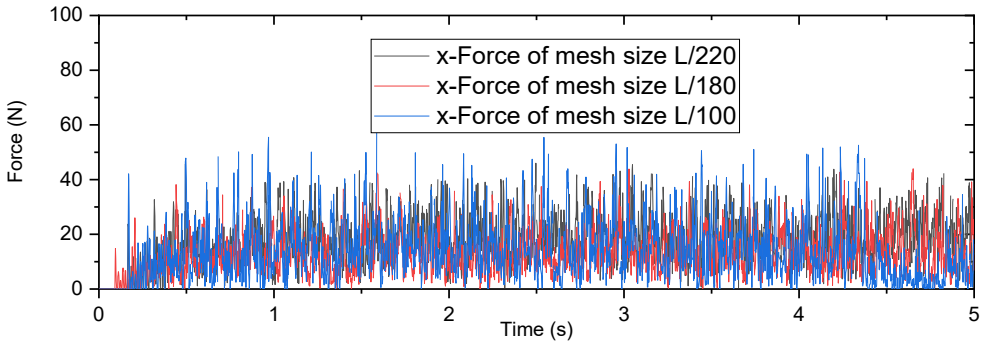

Fig. 16. The icebreaking force in the x-direction for different mesh size

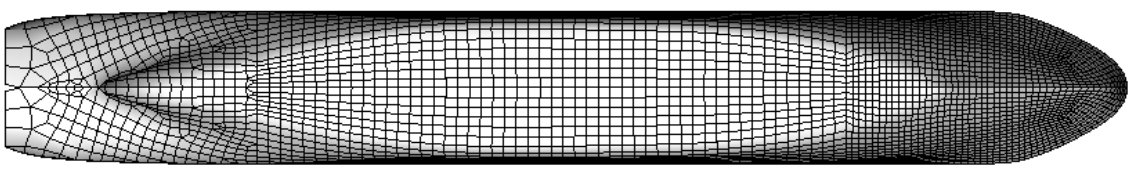

(a)

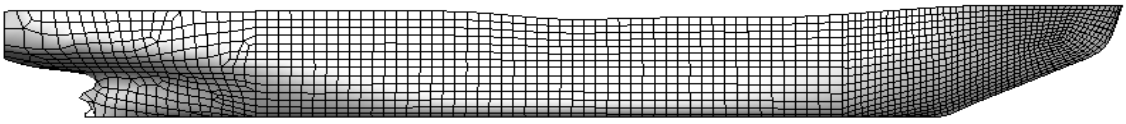

(b)

Fig. 17. The 3D model of icebreaker (a) top view of the numerical model; (b) side view of the numerical model

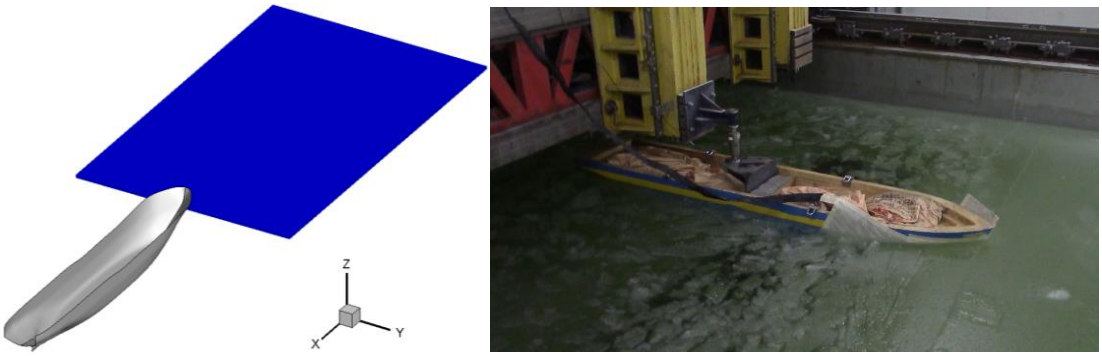

(a) (b)

Fig. 18. Configuration of the initial condition: (a) numerical model in level ice; (b) experiment in level ice

6.3 Icebreaking process

Fig.19, which includes snapshots from the ice tanker test and the numerical calculation, shows the continuous icebreaking process at the speed of 0.410 m/s. In order to better observe ice damage, the hull is set to be translucent. The ice crushing process starts upon ice-hull contact. As described by Liu (2009), a crushing process occurs before the ice is bent to broken ice floes. This is observed at the initial contact stage t = 1.88 s (Fig. 19(a)) when the icebreaker contacts the ice layer: local crushing failure of ice occurs at bow stem. The local damage of the ice sheet close to the bow stem is serious since crushing failure is severer than bending failure (see Fig. 15), so it showed in red colour in the numerical result (as shown in Fig. 19 (a)). While the vertical component of icebreaking force is insufficient to cause bending failure (generally shaped in the circumferential crack), the ice continues to be damaged in crushing mode (also as shown in Fig. 19 (a)). In Fig. 19 (b), with the icebreaker going forward, a new bending crack forms due to the propagation of the last bending crack. Simultaneously, a large-scale circumferential crack at both sides of the hull is propagating towards the bow stem, just as the same as the snapshot of the test video.

Along with time, cracks propagate, and the ice sheet is broken into small cracked ice. The crushed ice floes (close to red-colored floes) and bent ice floes (close to green colored floes) are pushed to both sides of the ship hull, and an icebreaking channel formed behind the ship body, which can be found in Fig. 19 (c). Ice floes keep twirling along the hull edge with the influence of the icebreaker navigation till they parallel with the hull, followed by submerging and sliding. Finally, the floes break contact with the hull. Crushing is likely to be the unique failure mode in some zones, usually at the bow and shoulders, where there are large slope angles (almost vertical) (Lindqvist, 1989). However, since water is not taken into account in the simulation, the ice floes drop down instead of floating around the hull. The investigation model for ice floes rotating and submerging in the water at the next icebreaking stage will be established in future work.

In this case, the crushing failure, bending failure, and mixed failure mode, as well as crack propagation in the icebreaking process, are well simulated by the PD numerical method. The broken ice floes are the basis to further study forces from submersion and hydrodynamics, while most of the other methods can only calculate them by empirical formulas (Li et al., 2018a; Myland et al., 2019). This demonstrates the effectiveness of the present numerical method for modelling the failure process of ice-ship interaction.

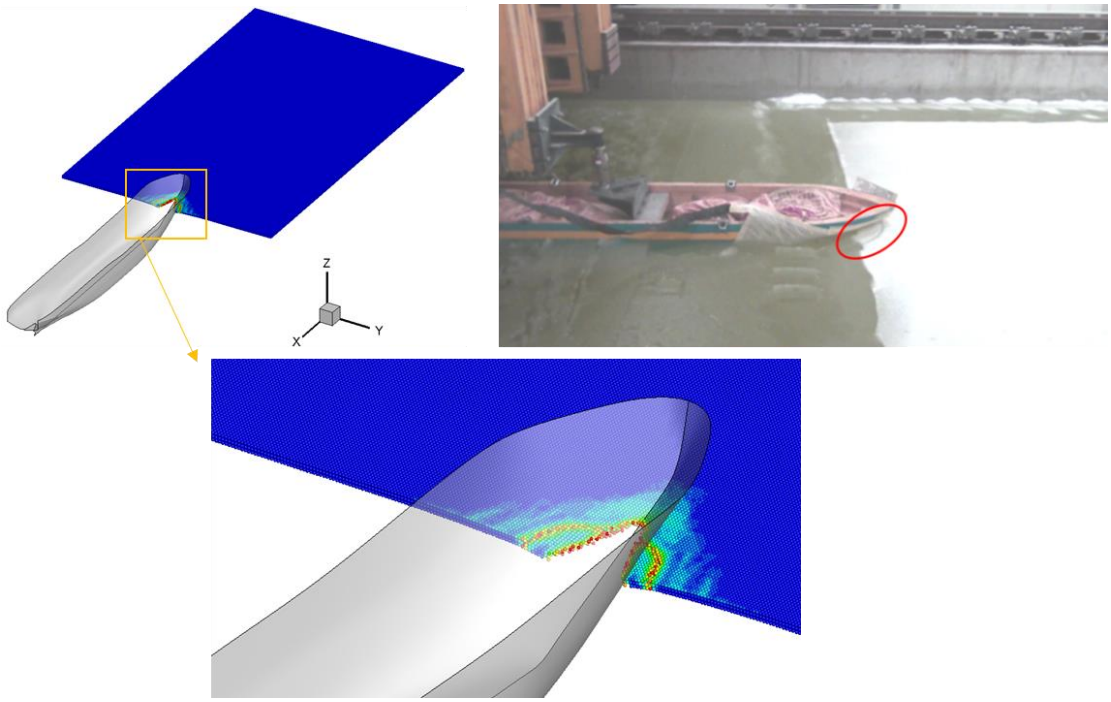

(a)

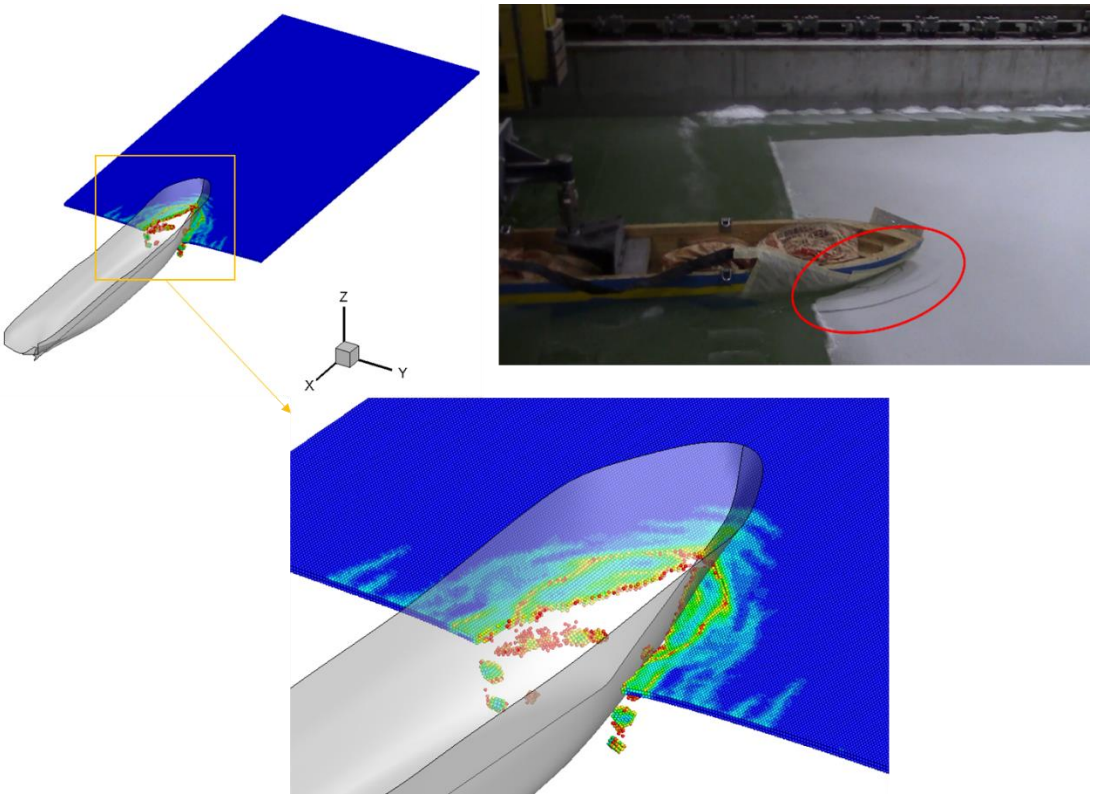

(b)

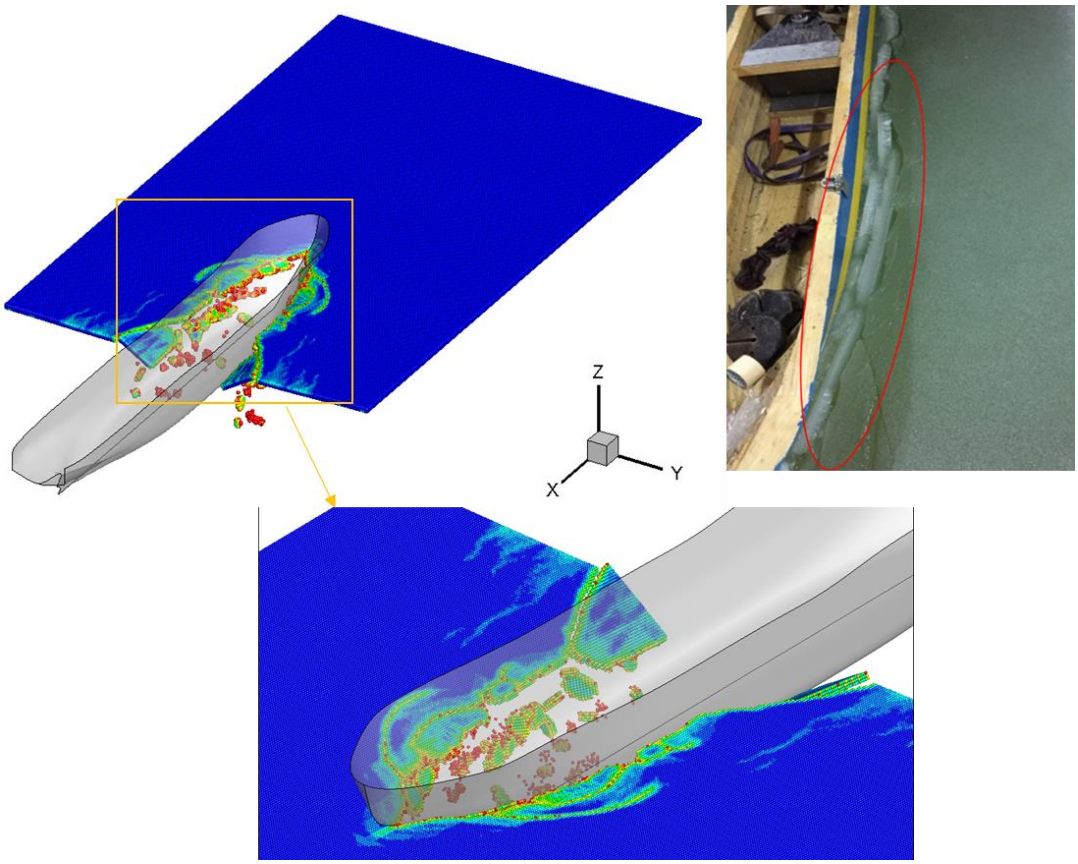

(c)

Fig. 19. Icebreaking process of field, experimental and numerical icebreaking process (a) Initial contact stage t = 1.88 s (b) Crack propagation stage) t = 4.14 s (c) Mixed failure mode stage t = 10.16 s

Detailed observation of the icebreaking pattern at different parts of the ship was captured by test videos and the present numerical simulation, which shows a good agreement in the phenomenon of the icebreaking pattern. Fig. 20 gives the comparison of the detailed icebreaking pattern between diagrammatic sketches observed in the model tests and snapshots captured in the present numerical simulation. It is observed that bending damage, which is mainly caused by the formation and evolution of circumferential cracks, plays a critical role in the failure mode during all tests by Huang et al. (2018). The computational results visualized a similar phenomenon. The cycle process of ice failure mode in the icebreaking process begins with the initial appearance of a long circumferential crack.

It is noticeable that, in the model experiment, the circumferential cracks on both sides are symmetrical in the

middle longitudinal section with non-simultaneous development behaviour. However, this is completely symmetric in the numerical simulation due to the assumption of isotropic in the ice model. It is visualized the formation of radial crack, which is extended from the position of half breadth in the bow region, breaks the propagation of the initial circumferential crack. Meanwhile, other breaking patterns were captured successively and successfully. The local crushing events, occurring from stem to position of quarter breadth, is accompanied by the appearance of a secondary circumferential crack. This kind of crack is almost paralleled the bow shape line, and its direction of travel develops to the stem. There appears a short circumferential crack near the bow, which leads to the ice was cut into small cusps. The present numerical method developed in this paper has captured most of the icebreaking patterns in the real ice–ship interaction process.

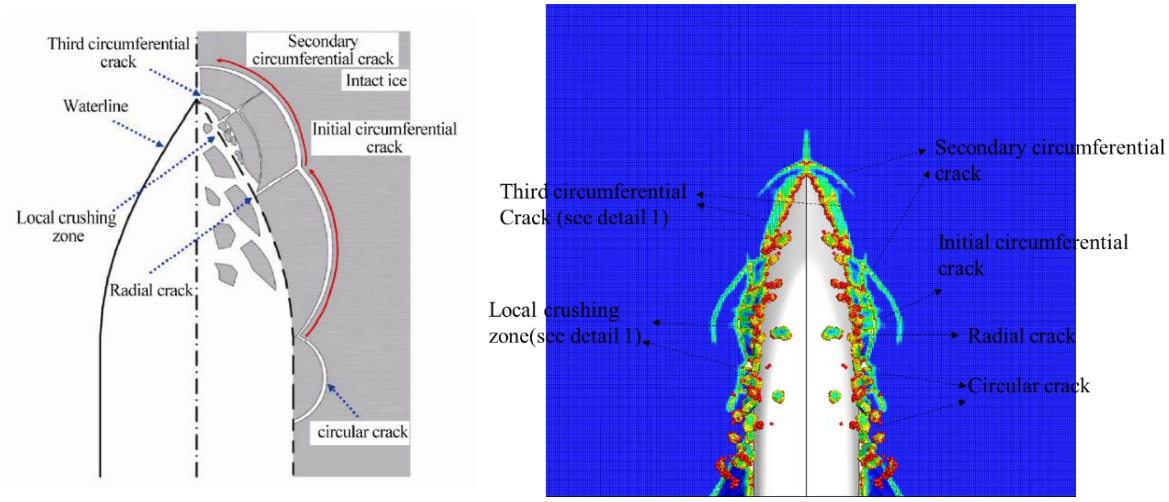

(a) (b)

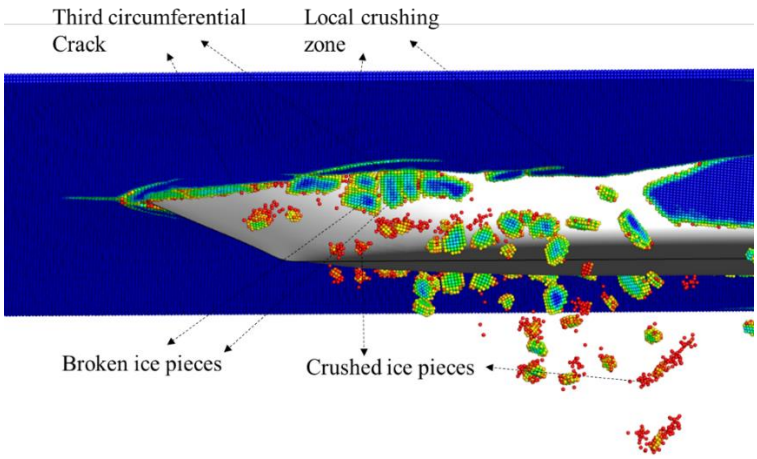

(c)

Fig. 20. Illustration of icebreaking patterns along the vessel (a) schematic diagram for the experiment (Huang et al., 2016) (b) snapshot for numerical simulation form top view (c) snapshot of detail 1 in (b)

6.4 Icebreaking resistance

Since the longitudinal component of the global ice load is the main component of icebreaking resistance, the global ice force is the critical factor to help ship design for optimal performance (Riska, 2019). In general, the ice load prediction process should distinguish between the maximum force and the average force. However, the effect of the maximum ice force is reduced by the inertia of the ship during icebreaking (Riska, 2011). Therefore, the icebreaking resistance is treated as the time average of the global (or total) ice load or its longitudinal component in most research work (e.g., (Su et al., 2011; Zhou, 2012),). In this paper, the comparison is made by the mean value of the numerical simulation, model test data, and the Lindqvist method. The icebreaking resistance in the model test is collected by tactile sensor measurements. With the consideration of the most decisive hull shape coefficient and its working condition, the Lindqvist method (Lindqvist, 1989) calculates total resistance by formulas based on experience data and physical analysis (Myland and Ehlers, 2016), making it the most popular approach. Lindqvist divided icebreaking resistance into two components of bending and crushing, which are (Lindqvist, 1989):

$$R_B = \frac{27}{64} \cdot \sigma_f \cdot B \cdot \frac{h_i^{1.5}}{\sqrt{\frac{E}{12(1-\upsilon^2)g\rho_w}}} \cdot (\tan\psi + \frac{\mu\cos\phi}{\cos\psi\sin\alpha}) \cdot (1 + \frac{1}{\cos\psi}) \tag{26}$$

$$R_C = 0.5\sigma_f h_i^2 \cdot \frac{\tan\phi + \mu\frac{\cos\phi}{\cos\psi}}{1 - \mu\frac{\sin\phi}{\cos\psi}} \tag{27}$$

$$\psi = \arctan\frac{\tan\varphi}{\sin\alpha} \tag{28}$$

where R_B is the bending resistance, σ_f the flexural strength, B the ship breadth, h_i the ice thickness, υ the Poisson's ratio, ρ_w the density of water, g the gravitational acceleration, ψ the normal angle, μ the friction

coefficient between ship hull and ice, R_C the crushing resistance. The normal angle is calculated from the waterline entrance angle and the stem angle according to Eq. (28). Then, the breaking force is calculated:

$$R_{br} = (R_C + R_B) \cdot (1 + \frac{1.4V}{\sqrt{gh_i}}) \tag{29}$$

The time histories of icebreaking resistance of an icebreaker sailing with forwarding speed 0.410 m/s are shown in Fig. 21. Because the hull, ice model and contact position of the numerical calculation process are completely symmetrical, the force in the y-axis direction is equal to zero. The ice loads history in the continuous icebreaking process is obviously periodic, stochastic and impulsive. The global ice load usually fluctuates in a period of time, while the maximum ice load only appears in an extremely short period of time. It can be seen that the force in the longitudinal component (z-axis) shown in Fig. 21 (b) is much higher than a component in the x direction shown in Fig. 21 (a), and it is almost equal to the total force shown in Fig. 21 (c). This is clear evidence that the ice load in the z-direction is the main component of the icebreaking resistance, which is caused by the lifting force from ice bending failure.

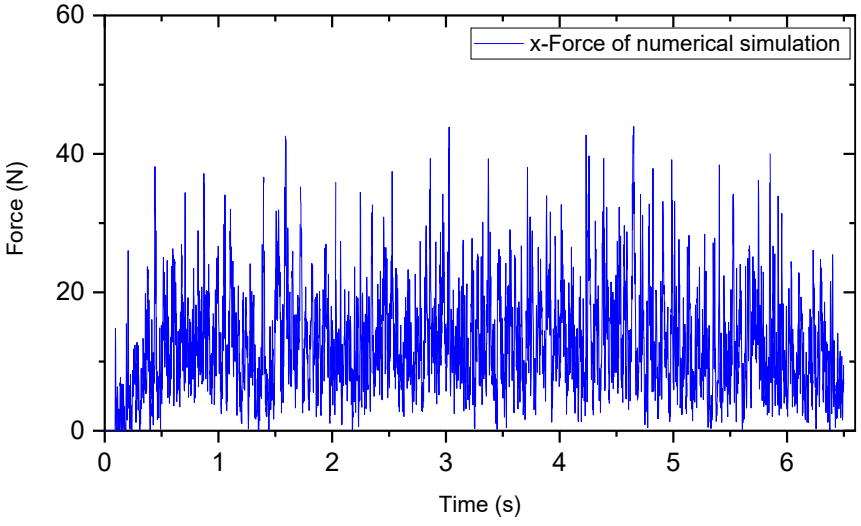

(a) Historical force-time curve in the *x*-axis

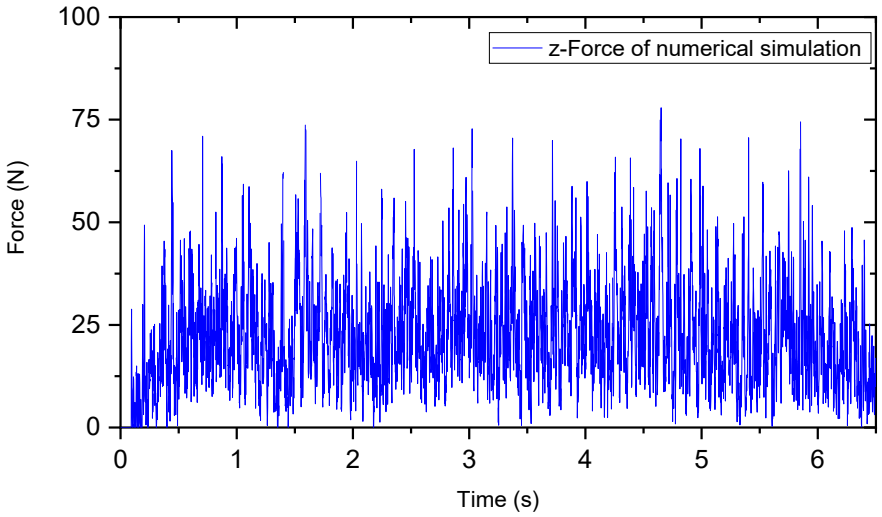

(b) Historical force-time curve in the *z*-axis

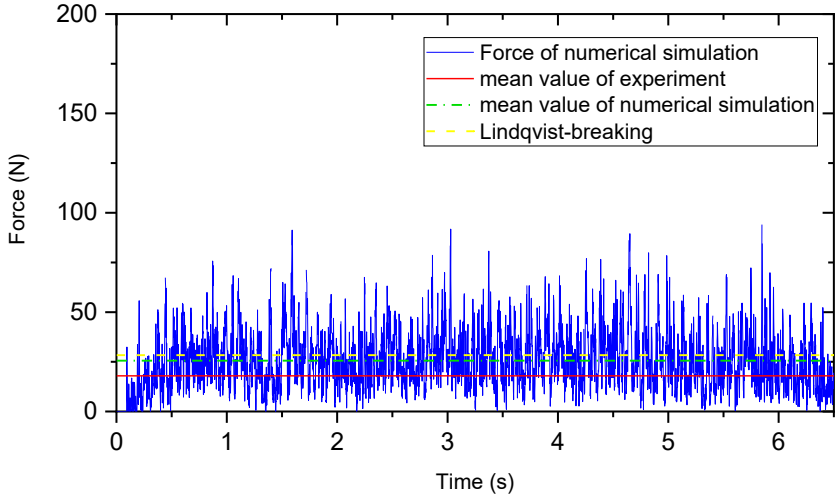

(c) Historical force-time curve

Fig. 21. Historical force-time curve at a speed of 0.410 m/s (a) Historical force-time curve in the x-axis (b) Historical force-time curve in z-axis (c) Historical force-time curve

The other four velocity conditions including 0.082 m/s, 0.164 m/s, 0.246 m/s and 0.328 m/s are shown in Fig. 22 to Fig. 25. It is found that the mean values of ice resistance in the present numerical simulation are slightly larger than those in the model test. The main reason may be that the vertical contact force for ice sliding down is calculated in the contact detection process.

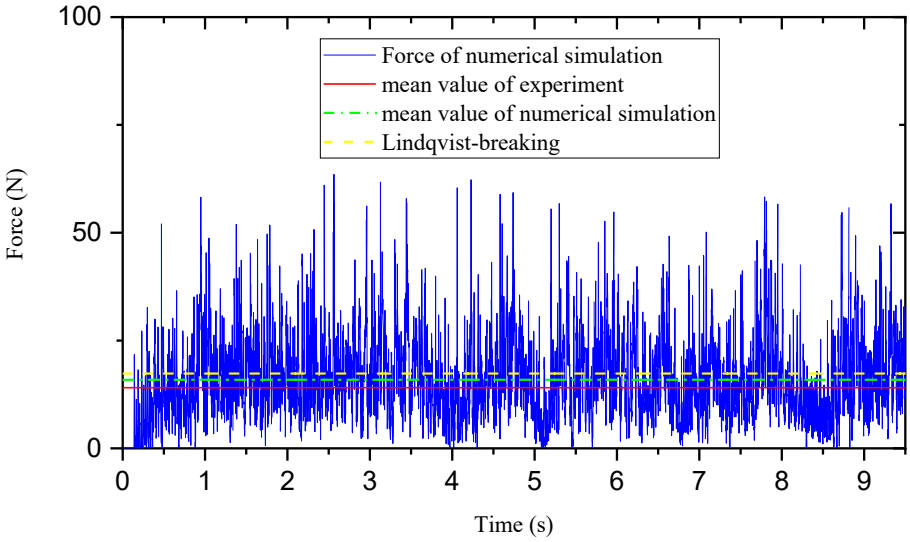

Fig. 22. Historical force-time curve at a speed of 0.082 m/s

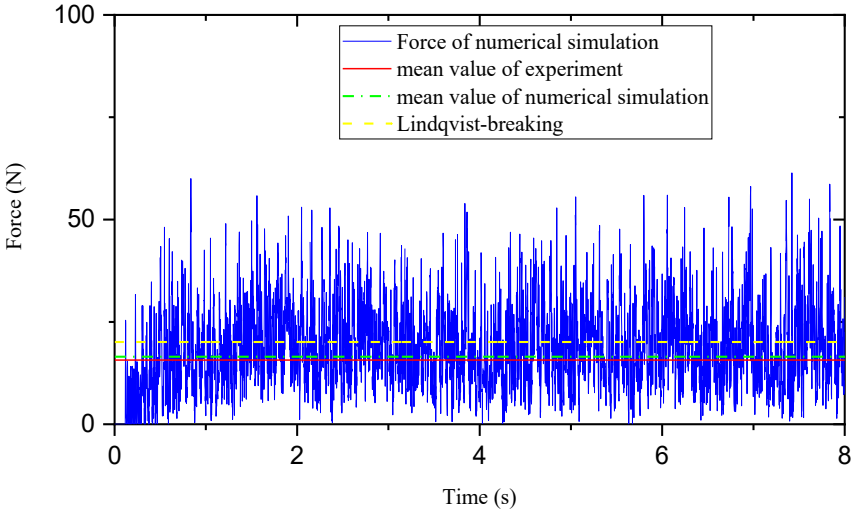

Fig. 23. Historical force-time curve at a speed of 0.164 m/s

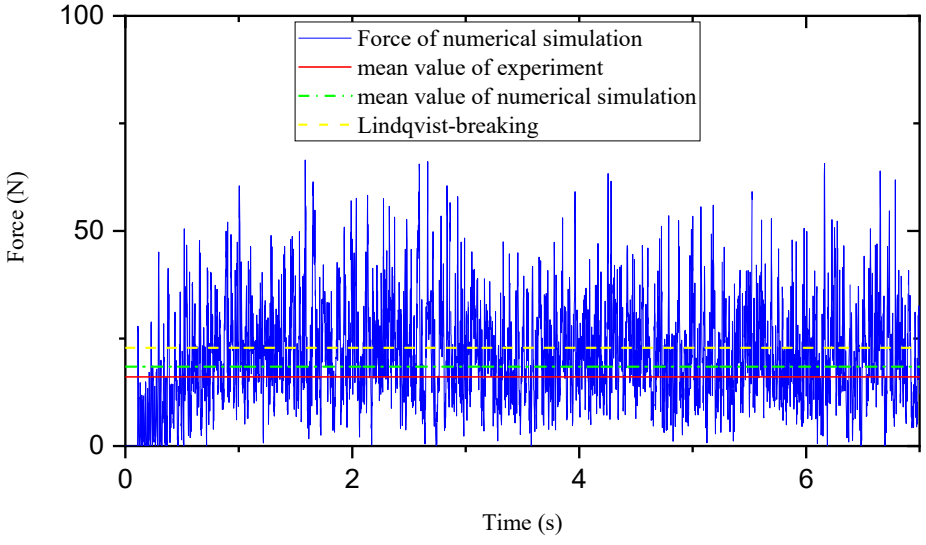

Fig. 24. Historical force-time curve at a speed of 0.246 m/s

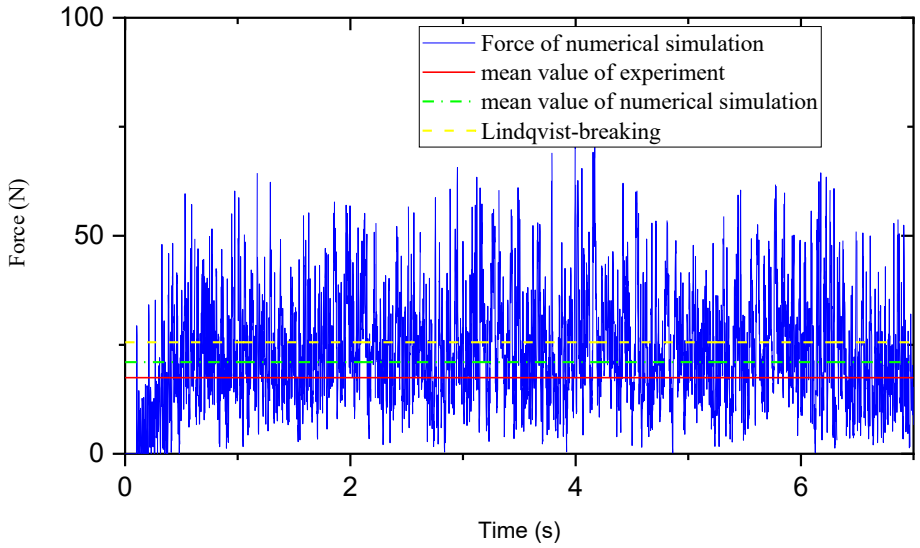

Fig. 25. Historical force-time curve at a speed of 0.328 m/s

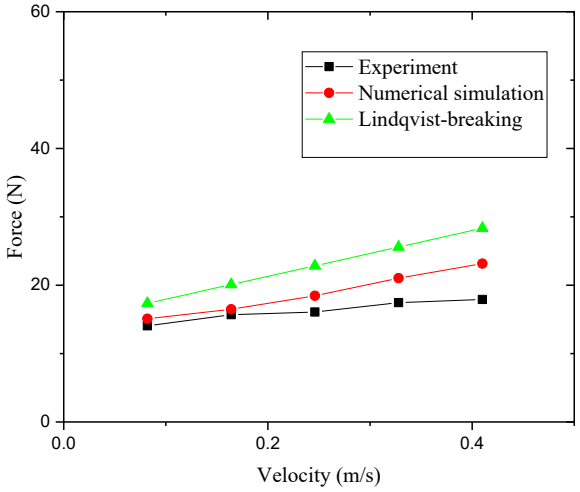

Fig. 26. Comparison of icebreaking resistance in terms of different ship velocities

The comparison of icebreaking resistance is plotted with navigating velocity among the present numerical simulation, experiment results, and Lindqvist calculation in Fig. 26. The results of the numerical simulation are obtained by averaging the corresponding icebreaking resistance from Fig. 22 (c) to Fig. 25. Although the rate of resistance increasing with a forward speed in the numerical calculation is closer to that of the Lindqvist method, and the increasing trend with navigating speed is in good agreement in all three methods. Moreover, the present numerical results are in notably better agreement with the experimental measurements.

7. Conclusion

In this paper, the ice is modelled by the nonlocal particle PD method, and the continuous contact detection algorithm for ice-ship interaction is introduced to investigate the icebreaking process in level ice. The contact detection algorithm is more suitable for the interaction of a complex structure surface and particles. The predicted stress-time history and ice behaviour of the ice bending process are consistent with the experimental results. The computational damage mode of the ice sphere impact case is qualitatively agreed with that observed in the experiment.

The validated PD model is applied to ice-structure interaction investigating the ice damage pattern and icebreaking resistance of an icebreaker sailing in level ice. Good agreement between the present numerical results and the experimental data demonstrates the good performance of the present PD model in terms of accuracy and visualization.

As one of the highlights in the present approach, the crack generation is obtained naturally without setting pre-existing crack at impact simulation, though it is also acknowledged that the damage initiation should be included in future work. In addition, the present numerical model ignored ship motion and the influence of water, subsequential researches are required to including these important issues for improved numerical modelling, such as the hydrodynamic effect on interaction process and efficient parallel computation.

Acknowledgements

The authors gratefully acknowledge financial support from Harbin Engineering University. This research was also supported by the National Natural Science Foundation of China (Grant No. 51679052 and No. 51809055),

References:

Das, J., 2017. Modeling and Validation of Simulation Results of an Ice Beam in Four-Point Bending Using Smoothed Particle Hydrodynamics.

International Journal of Offshore and Polar Engineering 27 (1), 82-89.

Das, J., Polić, D., Ehlers, S., Amdahl, J., 2014. Numerical Simulation of an Ice Beam in Four-Point Bending Using SPH, ASME 2014 33rd International Conference on Ocean, Offshore and Arctic Engineering.

Derradji-Aouat, A., 2003. Multi-surface failure criterion for saline ice in the brittle regime. Cold Regions Science and Technology 36 (1-3), 47-70.

Derradji-Aouat, A., van Thiel, A., 2004. Terry Fox Resistance Tests–Phase III (PMM Testing). The ITTC Experimental Uncertainty Analysis Initiative. NRC/IOT Report TR-2004-05, National Research Council of Canada, Institute for Ocean Technology, St. John's, NL, Canada.

Erceg, S., Ehlersa, S., 2017. Semi-empirical level ice resistance prediction methods. Ship Technology Research 64 (1), 1-14.

Gao, Y., Hu, Z., Ringsberg, J.W., Wang, J.J.O.E., 2015. An elastic–plastic ice material model for ship-iceberg collision simulations. 102, 27-39.

Gao, Y., Oterkus, S., 2018. Ordinary state-based peridynamic modelling for fully coupled thermoelastic problems. Continuum Mechanics and Thermodynamics 31 (4), 907-937.

Gao, Y., Oterkus, S., 2020. Fluid-elastic structure interaction simulation by using ordinary state-based peridynamics and peridynamic differential operator. Engineering Analysis with Boundary Elements 121, 126-142.

Guo, C., Xie, C., Wang, S., Li, X., Luo, W., 2016. Resistance of ships in pack ice conditions. Harbin Gongcheng Daxue Xuebao/Journal of Harbin Engineering University 37 (4), 481-486.

Hu, W.K., Ha, Y.D., Bobaru, F., Silling, S.A., 2012. The formulation and computation of the nonlocal J-integral in bond-based peridynamics. International Journal of Fracture 176 (2), 195-206.

Huang, Y., Huang, S.Y., Sun, J.Q., 2018. Experiments on navigating resistance of an icebreaker in snow covered level ice. Cold Regions Science and Technology 152, 1-14.

Huang, Y., Sun, J.Q., Ji, S.P., Tian, Y.K., 2016. Experimental Study on the Resistance of a Transport Ship Navigating in Level Ice. Journal of Marine Science and Application 15 (2), 105-111.

Javili, A., Morasata, R., Oterkus, E., Oterkus, S., 2019. Peridynamics review. Mathematics and Mechanics of Solids 24 (11), 3714-3739.

Jeong, S.Y., Choi, K., Kang, K.J., Ha, J.S., 2017. Prediction of ship resistance in level ice based on empirical approach. International Journal of Naval

Architecture and Ocean Engineering 9 (6), 613-623.

Ji, S.Y., Wang, A.L., Su, J., Yue, Q.J., 2011. Experimental Studies on Elastic Modulus and Flexural Strength of Sea Ice in the Bohai Sea. Journal of cold regions engineering 25 (4), 182-195.

Jordaan, I.J., 2001. Mechanics of ice-structure interaction. Engineering fracture mechanics 68 (17-18), 1923-1960.

Kämäräinen, J., 1993. Evaluation of ship ice resistance calculation methods. Licentiate's thesis. Helsinki University of Technology, Faculty of Mechanical Engineering.

Keinonen, A., 1996. Icebreaker characteristics synthesis.

Lau, M., 2006. Discrete element modeling of ship manoeuvring in ice.

Lee, T.K., Lee, J.H., Kim, H., Rim, C.W., 2014. Field measurement of local ice pressures on the ARAON in the Beaufort Sea. International Journal of Naval Architecture and Ocean Engineering 6 (4), 788-799.

Li, F., Goerlandt, F., Kujala, P., Lehtiranta, J., Lensu, M., 2018a. Evaluation of selected state-of-the-art methods for ship transit simulation in various ice conditions based on full-scale measurement. Cold Regions Science and Technology 151, 94-108.

Li, F., Kotilainen, M., Goerlandt, F., Kujala, P., 2019. An extended ice failure model to improve the fidelity of icebreaking pattern in numerical simulation of ship performance in level ice. Ocean Engineering 176, 169-183.

Li, H., Yang, Z., Feng, Y., Wang, Y.-B., Wang, S.-Y., 2018b. Study on the Influence of Ice-Water Coupling on Numerical Calculation of Ice Load, ASME 2018 37th International Conference on Ocean, Offshore and Arctic Engineering. American Society of Mechanical Engineers.

Lindqvist, G., 1989. A STRAIGHTFORWARD METHOD FOR CALCULATION OF ICE RESISTANCE OF SHIPS, POAC 89, 10th Intl Conference, Port and Ocean Engineering under Arctic Conditions, Luleaa, Sweden.

Liu, J., 2009. Mathematical modeling ice-hull interaction for real time simulations of ship manoeuvring in level ice. Memorial University of Newfoundland.

Liu, J., Lau, M., Williams, F.M., 2006. Mathematical modeling of ice-hull interaction for ship maneuvering in ice simulations, Proceedings of 7th International Conference and Exhibition on Performance of Ships and Structures in Ice (ICETECH), Banff, Alberta, Canada.

Liu, M.H., Wang, Q., Lu, W., 2017. Peridynamic simulation of brittle-ice crushed by a vertical structure. International Journal of Naval Architecture and Ocean Engineering 9 (2), 209-218.

Liu, R., Yan, J., Li, S., 2019. Modeling and simulation of ice–water interactions by coupling peridynamics with updated Lagrangian particle hydrodynamics. Computational Particle Mechanics 7 (2), 241-255.

Liu, R.W., Xue, Y.Z., Lu, X.K., Cheng, W.X., 2018. Simulation of ship navigation in ice rubble based on peridynamics. Ocean Engineering 148, 286-298.

Lu, W., Wang, Q., Jia, B., Shi, L., 2018. Simulation of Ice-Sloping Structure Interactions With Peridynamic Method, The 28th International Ocean and Polar Engineering Conference. International Society of Offshore and Polar Engineers.

Lubbad, R., Loset, S., 2011. A numerical model for real-time simulation of ship-ice interaction. Cold Regions Science and Technology 65 (2), 111-127.

Madenci, E., Dorduncu, M., Barut, A., Phan, N., 2018. A state-based peridynamic analysis in a finite element framework. Engineering fracture mechanics 195, 104-128.

Madenci, E., Dorduncu, M., Gu, X., 2019. Peridynamic least squares minimization. Computer Methods in Applied Mechanics and Engineering 348, 846-874.

Madenci, E., Oterkus, E., 2014. Peridynamic Theory and Its Applications.

Madenci, E., Oterkus, S., 2017. Ordinary state-based peridynamics for thermoviscoelastic deformation. Engineering fracture mechanics 175, 31-45.

Majid, I., Menon, B., 1983. INVESTIGATIVE STUDY OF SIMULATION TECHNIQUES AND NAVIGATION PROBLEMS FOR THE ARCTIC MARINE ENVIRONMENT.

Molyneux, D., 2017. Model Ice: A Review of its Capacity and Identification of Knowledge Gaps, ASME 2017 36th International Conference on Ocean, Offshore and Arctic Engineering. American Society of Mechanical Engineers.

Molyneux, W., Kim, H., 2007. Model experiments to support the design of large icebreaking tankers.

Monaghan, J., 1985. Particle methods for hydrodynamics. Computer Physics Reports 3 (2), 71-124.

Myland, D., Ehlers, S., 2016. Influence of bow design on ice breaking resistance. Ocean Engineering 119, 217-232.

Myland, D., Ehlers, S.J.S., Structures, O., 2019. Investigation on semi-empirical coefficients and exponents of a resistance prediction method for ships sailing ahead in level ice. 1-10.

Nezami, E.G., Hashash, Y.M.A., Zhao, D.W., Ghaboussi, J., 2004. A fast contact detection algorithm for 3-D discrete element method. Computers and Geotechnics 31 (7), 575-587.

Oterkus, S., Madenci, E., Agwai, A., 2014. Fully coupled peridynamic thermomechanics. Journal of the Mechanics and Physics of Solids 64, 1-23.

Palmer, A., Dempsey, J., 2009. Model tests in ice, Proceedings of the International Conference on Port and Ocean Engineering Under Arctic Conditions.

Parks, M.L., Lehoucq, R.B., Plimpton, S.J., Silling, S.A., 2008. Implementing peridynamics within a molecular dynamics code. Computer Physics Communications 179 (11), 777-783.

Pashazad, H., Kharazi, M., 2019. A peridynamic plastic model based on von Mises criteria with isotropic, kinematic and mixed hardenings under cyclic loading. International Journal of Mechanical Sciences 156, 182-204.

Ren, H., Zhuang, X., Rabczuk, T., 2017. Dual-horizon peridynamics: A stable solution to varying horizons. Computer Methods in Applied Mechanics and Engineering 318, 762-782.

Ren, H., Zhuang, X., Rabczuk, T., Zhu, H., 2019. Dual-support smoothed particle hydrodynamics in solid: variational principle and implicit formulation. Engineering Analysis with Boundary Elements 108, 15-29.

Riska, K., 2011. Ship–ice interaction in ship design: Theory and practice. Course Material NTNU.

Riska, K., 2019. DESIGN OF ICE BREAKING SHIPS.

Riska, K., Leiviskä, T., Nyman, T., Fransson, L., Lehtonen, J., Eronen, H., Backman, A., 2001. Ice performance of the Swedish multi-purpose icebreaker Tor Viking II, Proceedings of the International Conference on Port and Ocean Engineering Under Arctic Conditions.

Riska, K., Wilhelmson, M., Englund, K., Leiviskä, T.J.S.L., Winter Navigation Research Board, Helsinki University of Technology, Espoo, Finland, Research Report, 1997. Performance of Merchant vessels in the Baltic. (52).

Ruestes, C., Tramontina, D., Bringa, E., 2014. Impact Studies with Peridynamics.

Sawamura, J., 2018. 2D numerical modeling of icebreaker advancing in ice-covered water. International Journal of Naval Architecture and Ocean

Engineering 10 (3), 385-392.

Sawamura, J., Kioka, S., Konno, A., 2015. Experimental and numerical investigation on ice submerging for icebreaker with 2D model test using synthetic ice, Proceedings of the International Conference on Port and Ocean Engineering Under Arctic Conditions.

Sawamura, J., Riska, K., Moan, T., 2009. Numerical simulation of breaking patterns in level ice at ship's bow, The Nineteenth International Offshore and Polar Engineering Conference. International Society of Offshore and Polar Engineers.

Sawamura, J., Yamauchi, Y., Anzai, K., 2017. Simulation of Ice Force and Breaking Pattern for Icebreaking Ship in Level Ice, ASME 2017 36th International Conference on Ocean, Offshore and Arctic Engineering. American Society of Mechanical Engineers.

Schulson, E.M., 1990. The brittle compressive fracture of ice. Acta Metallurgica et Materialia 38 (10), 1963-1976.

Schulson, E.M., 1999. The structure and mechanical behavior of ice. JOM 51 (2), 21-27.

Schulson, E.M., 2001. Brittle failure of ice. Engineering fracture mechanics 68 (17-18), 1839-1887.

Shi, Y., 2002. Model test data analysis of ship maneuverability in ice. Memorial University of Newfoundland.

Silling, S.A., 2000. Reformulation of elasticity theory for discontinuities and long-range forces. Journal of the Mechanics and Physics of Solids 48 (1), 175-209.

Silling, S.A., Askari, E., 2005. A meshfree method based on the peridynamic model of solid mechanics. Computers & Structures 83 (17-18), 1526-1535.

Silling, S.A., Epton, M., Weckner, O., Xu, J., Askari, E., 2007. Peridynamic States and Constitutive Modeling. Journal of Elasticity 88 (2), 151-184.

Sodhi, D.S., Griggs, D.B., Tucker, W.B., 2001. Ice performance tests of USCGC Healy, Proceedings of the International Conference on Port and Ocean Engineering Under Arctic Conditions.

Song, Y., Yu, H., Kang, Z., 2019. Numerical study on ice fragmentation by impact based on non-ordinary state-based peridynamics. Journal of Micromechanics and Molecular Physics 04 (01), 1850006.

Su, B., 2011. Numerical predictions of global and local ice loads on ships, Department of Marine Technology.

Su, B., Riska, K., Moan, T., 2011. Numerical study of ice-induced loads on ship hulls. Marine Structures 24 (2), 132-152.

Tan, X., 2014. Numerical Investigation of Ship's Continuous-Mode Icebreaking in Level Ice.

Timco, G., Weeks, W., technology, 2010. A review of the engineering properties of sea ice. Cold Regions Science & Technology 60 (2), 107-129.

Tippmann, J.D., 2011. Development of a strain rate sensitive ice material model for hail ice impact simulation. UC San Diego.

Tippmann, J.D., Kim, H., Rhymer, J.D., 2013. Experimentally validated strain rate dependent material model for spherical ice impact simulation. International Journal of Impact Engineering 57, 43-54.

Valanto, P., 2001. The resistance of ships in level ice.

Vazic, B., Diyaroglu, C., Oterkus, E., Oterkus, S., 2020. Family Member Search Algorithms for Peridynamic Analysis. Journal of Peridynamics and Nonlocal Modeling 2 (1), 59-84.

Vazic, B., Oterkus, E., Oterkus, S., 2019. Peridynamic approach for modelling ice-structure interactions, Trends in the Analysis and Design of Marine Structures: Proceedings of the 7th International Conference on Marine Structures CRC Press, Dubrovnik, Croatia.

Wang, B.Q., Oterkus, S., Oterkus, E., 2020. Determination of horizon size in state-based peridynamics. Continuum Mechanics and Thermodynamics.

Wang, C., Ren, H.L., Li, H., 2014. A Finite Element Method to Simulate Ice Based on Multi-Surface Failure Criterion. Applied Mechanics and Materials 623, 90-96.

Wang, C., Xiong, W.P., Chang, X., Ye, L.Y., Li, X., 2018a. Analysis of variable working conditions for propeller-ice interaction. Ocean Engineering 156, 277-293.

Wang, Q., Wang, Y., Zan, Y., Lu, W., Bai, X., Guo, J., 2018b. Peridynamics simulation of the fragmentation of ice cover by blast loads of an underwater explosion. Journal of Marine Science and Technology 23 (1), 52-66.

Wang, S., 2001. A dynamic model for breaking pattern of level ice by conical structures. Acta Polytechnica Scandinavica Mechanical Engineering Me 156.

Williams, F., Spencer, D., 1992. Full scale trials in level ice with Canadian R-Class icebreaker.

Ye, L.Y., Guo, C.Y., Wang, C., Wang, C.H., Chang, X., 2019. Peridynamic solution for submarine surfacing through ice. Ships and Offshore Structures 15 (5), 535-549.

Ye, L.Y., Wang, C., Chang, X., Zhang, H.Y., 2017. Propeller-ice contact modeling with peridynamics. Ocean Engineering 139, 54-64.

Zhang, N.B., Zheng, X., Ma, Q.W., 2017. Updated Smoothed Particle Hydrodynamics for Simulating Bending and Compression Failure Progress of Ice. Water 9 (11), 882.

Zhang, N.B., Zheng, X., Ma, Q.W., Hu, Z.H., 2019. A numerical study on ice failure process and ice-ship interactions by Smoothed Particle Hydrodynamics. International Journal of Naval Architecture and Ocean Engineering 11 (2), 796-808.

Zhang, Y., Wang, C., Guo, C., Tao, L., 2020. Peridynamic Analysis of Fragmentation of Ice Plate Under Explosive Loading With Thermal Effects, ASME 2020 39th International Conference on Ocean, Offshore and Arctic Engineering.

Zhou, L., 2012. Numerical and experimental investigation of stationkeeping in level ice.

Zhou, L., Chuang, Z.J., Bai, X., 2018. Ice forces acting on towed ship in level ice with straight drift. Part II: Numerical simulation. International Journal of Naval Architecture and Ocean Engineering 10 (2), 119-128.

Zhou, Q., Peng, H., Qiu, W., 2016. Numerical investigations of ship-ice interaction and maneuvering performance in level ice. Cold Regions Science and Technology 122, 36-49.